Computational Materials Science 51 (2012) 455–481

Contents lists available at SciVerse ScienceDirect

Computational Materials Science

journal homepage: www.elsevier.com/locate/commatsci

Investigating variability of fatigue indicator parameters of two-phase nickel-based superalloy microstructures

Bin Wen, Nicholas Zabaras *

Materials Process Design and Control Laboratory, Sibley School of Mechanical and Aerospace Engineering, Cornell University, Ithaca, NY 14853-3801, USA

ARTICLE INFO

Article history:
Received 19 May 2011
Received in revised form 23 July 2011
Accepted 28 July 2011
Available online 9 September 2011

Keywords:
Fatigue property
Two-phase superalloys
Polycrystalline microstructure
Model reduction
Principal component analysis
Polynomial chaos expansion
Stochastic simulation
Adaptive sparse grid collocation

ABSTRACT

Variability of fatigue properties of Nickel-based superalloys induced by microstructure feature uncertainties is investigated. The microstructure at one material point is described by its grain size and orientation features, as well as the volume fraction of the γ' phase. Principal component analysis (PCA) is introduced to reduce the dimensionality of the microstructure feature space. PCA and kernel PCA (KPCA) techniques are presented and compared. Reduced representations of input features are mapped to uniform or standard Gaussian distributions through polynomial chaos expansion (PCE) so that the sampling of new microstructure realizations becomes feasible. A crystal plasticity constitutive model is adopted to evaluate fatigue properties of two-phase superalloy microstructures under cyclic loading. The fatigue properties are measured by strain-based fatigue indicator parameters (FIP). Adaptive sparse grid collocation (ASGC) and Monte Carlo (MC) methods are used to establish the relation between microstructure feature uncertainties and the variability of macroscopic properties. Convergence with increasing dimensionality of the reduced surrogate stochastic space is studied. Distributions of FIPs and the convex hulls describing the envelope of these parameters in the presence of microstructure uncertainties are shown.

1. Introduction

Quantification of mechanical property variability of microstructures has been studied extensively as it is essential for the prediction of extreme properties and microstructure-sensitive design of materials. In the past few years, a series of investigations were undertaken to study the variation in stress–strain response and elastic properties of single phase metals caused by microstructure uncertainties using a variety of computational methodologies. In [1], the principle of maximum entropy (MaxEnt) was used to describe the grain size distribution of polycrystals given a set of grain distribution moments as constraints. Microstructure realizations were then generated and interrogated using crystal plasticity finite element method (CPFEM) [2]. Orientations were randomly assigned to all constituent grains. The Monte Carlo (MC) method was adopted to compute the error-bars of effective stress–strain response of FCC aluminum. In [3], the orientation distribution function (ODF) was adopted to describe the polycrystalline microstructure. A number of ODF samples were given as the input data. The Karhunen-Loève expansion (KLE) [4,5] was utilized to reduce the input complexity and facilitate the high-dimensional stochastic simulation. An adaptive version of the sparse grid collocation strategy [6,7] was used to obtain the variability of the stress–strain curve and the convex hull of elastic modulus of FCC aluminum after deformation. Mechanical response variability and thermal properties due to both orientation and grain size uncertainties were analyzed in [8,9]. A non-linear model reduction technique based on manifold learning [10] has been introduced to find the surrogate space of the grain size feature while grain orientations were represented using KLE. Probabilistic stress response after deformation was constructed for FCC Nickel [8].

Most of the previous research focuses on elasto-plastic response and elastic properties of single phase polycrystals. Fatigue resistance is also of great importance in materials design. In addition, alloys composed of more than one constituent materials are widely used in components that require demanding properties in a high-temperature environment (e.g. aircraft-engines). Nickel-based superalloys are extensively used in turbine disks and blades [11]. Numerical tools have been developed for the understanding of the properties of Ni-based superalloys ranging from microscopic dislocation dynamics [12–17] to mesoscopic crystal plasticity models [18–21].

McDowell and colleagues conducted a series of studies on the properties (fatigue resistance and crack formation) of various Ni-based superalloys under cyclic loading [22–25]. Crystal plasticity constitutive models for homogenized ($\gamma + \gamma'$) grain and explicit two-phase (γ and γ') structures were developed and implemented in the finite element (FE) framework to investigate the

* Corresponding author. Fax: +1 607 255 1222.
E-mail address: zabaras@cornell.edu (N. Zabaras).
URL: http://mpdc.mae.cornell.edu/ (N. Zabaras).

0927-0256/$ - see front matter © 2011 Elsevier B.V. All rights reserved.
doi:10.1016/j.commatsci.2011.07.055

macroscopic stress–strain response and strain-based fatigue properties of superalloy microstructures. Effects of microstructure uncertainties on intrinsic fatigue resistance were emphasized [23,25,26]. An artificial neural network [27] was trained and applied to predict fatigue properties of microstructure given its features within the training bound [28].

In this work, our interest is in the variability of strain based fatigue indicator parameters (FIPs) [24] of Ni-based superalloy microstructures satisfying certain constraints. A set of microstructures described by their grain sizes, orientations and volume fraction of the γ' phase are provided as the initial database. Principal component analysis (PCA) model reduction techniques are applied to find low-dimensional representations of microstructure features and construct a surrogate space so that sampling of new microstructure features becomes computationally efficient. Both linear and non-linear (kernel) versions of PCA [29–31] are examined and compared. Polynomial chaos expansion (PCE) [5,32–34] is introduced to map the surrogate space to the support space of Gaussian or uniform random variables from which new samples can easily be drawn. The two-phase Ni-based superalloy constitutive model for IN 100 developed in [25] is adopted to predict the strain based FIPs of microstructures under cyclic loading. This model implicitly includes different type of γ' precipitates in a homogenized sense. The effects of γ' precipitates and grain size are introduced into the constitutive model by parameters such as volume fraction and equivalent diameters of primary, secondary, and tertiary precipitates. As a result, the two-phase microstructure is modeled by an equivalent homogenized single phase polycrystal microstructure. This is computationally convenient for applying model reduction techniques on microstructure features. Adaptive sparse grid collocation (ASGC) [7] is adopted to solve the underlying stochastic equations and construct the distribution of the properties of interest given the random input. Marginal distributions and convex hulls of FIPs are constructed and the correlation between FIPs is probed. The results are validated by comparing with MC simulations.

The organization of the paper is as follows. The representation of a microstructure and the mathematical framework of PCA/KPCA are briefly reviewed in Section 2. Emphasis is on the KPCA formulation. In Section 3, the polynomial chaos (PC) representation of the random variables is built. Homogenized superalloy polycrystal elasto-plasticity constitutive model along with the estimation of the FIPs are introduced as the deterministic simulator in Section 4. Numerical examples are presented in Section 5. The distributions and convex hulls of FIPs corresponding to certain statistically constrained microstructures are computed. Both MC and ASGC methods are adopted and convergence with increasing dimensionality of the reduced-order stochastic space is examined. Conclusions and discussion are provided in Section 6.

2. Construction of microstructure stochastic input model

2.1. Microstructure representation

Features of two-phase polycrystals include topology, texture (orientation of grains), and volume fraction of each phase. The microstructure topology is here defined in terms of grain shape and grain size [35]. For a polycrystalline alloy microstructure, its material properties are mostly determined by these three features. In order to model microstructure uncertainty, these features are considered as random variables. Appropriate mathematical descriptions of them are needed. A low-dimensional representation of the microstructure will be used as the stochastic surrogate input model to allow an efficient computation of the variability of the microstructure properties.

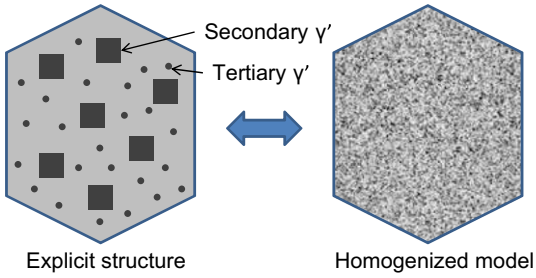

Fig. 1. Explicit structure of a $(\gamma + \gamma')$ grain and its equivalent homogenized model. The gray background on the left grain represents γ matrix, while secondary and tertiary γ' precipitates are depicted as dark particles.

The two-phase grain structure is modeled in a homogenized sense in this work. As a result, no γ' particles are explicitly modeled. Each constituent grain of the microstructure is considered as a homogenized single crystal which takes the effective properties of both phases. A schematic of an explicit $(\gamma + \gamma')$ structure of a grain and its equivalent homogenized model is demonstrated in Fig. 1. The effect of the second phase on material properties can be taken into account by introducing particular parameters in the constitutive model, which will be discussed in Section 5.

Statistical volume elements (SVEs) of polycrystalline alloy microstructures are represented as aggregates of discrete grains associated with specific orientations and phases (see Fig. 2a). As we implicitly model the two-phase material in a homogenized sense, each grain in the microstructure is effectively the combination of γ matrix and γ' precipitates aligning in the same orientation. An array containing both sizes and orientations of finite number of grains can be adopted as the descriptor of the microstructure (Fig. 2b). For a microstructure composed of M grains, the first M components of the feature array are sizes of homogenized grains sorted in ascending order and the rest $3M$ components are the corresponding orientations described by Rodrigues parameters [36], an axis-angle representation that consists of three components defined in Eq. (1):

$$\mathbf{r} = \mathbf{w}\tan\frac{\theta}{2}, \tag{1}$$

where $\mathbf{r} = \{r_1, r_2, r_3\}$ are the three Rodrigues components; $\mathbf{w} = \{w_1, w_2, w_3\}$ gives the direction cosines of the rotation axis with respect to microstructure coordinates; and θ is the rotation angle.

In [8], we have used a similar descriptor for single phase polycrystals. Model reduction was implemented for each feature and then combined to represent a microstructure. In this work, we will study the effects of each feature separately and determine the one that dominates fatigue properties of superalloy microstructures. We will start with a set of high-dimensional microstructure feature realizations represented by grain size and texture. These features will then be mapped to a low-dimensional space.

We are given a set of correlated microstructure realizations. In superalloy microstructures resulting from certain (e.g. deformation) process, the grain sizes, grain orientations (texture) and volume fraction of the γ phase satisfy certain (statistical) constraints. For grain size, the constraints are usually in the form of low-order statistical moments. The lognormal distribution is used often for describing polycrystalline Ni-based superalloy grain sizes [26]. The γ' phase disperses in the γ phase matrix as precipitates described by their size and volume fraction. Three types of γ', primary, secondary, and tertiary, are usually observed according to their size and other attributes. In the homogenized two-phase superalloy constitutive model, one needs in general to account for the γ'-phase uncertainty in addition to the grain size and orientation variation. The effect of microstructure features on fatigue

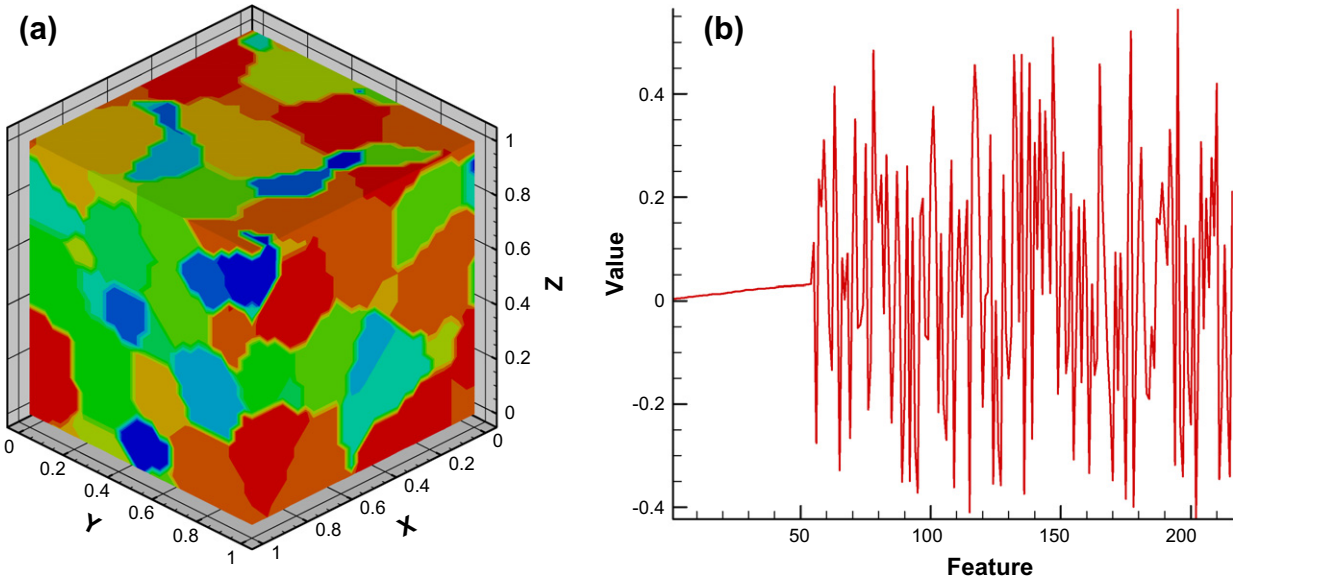

Fig. 2. (a) A 3D polycrystalline microstructure with 54 grains. (b) The descriptor of the microstructure. The first 54 components are the sizes of grains, and the last 162 components are Rodrigues parameters representing grain orientations.

properties can be studied using the deterministic material point simulator for different microstructure realizations.

2.2. Principal component analysis based model reduction

Stochastic microstructure representations are usually high-dimensional, which makes the stochastic simulation intractable. For example, a polycrystalline microstructure image containing 54 grains requires a 54-dimensional vector to store the grain size information (not accounting for any constraints). When grain orientations are included, this will end up to a 216-dimensional representation (Fig. 2b). To facilitate the stochastic simulation, model reduction techniques are introduced exploring the correlation among the data to construct a low-dimensional surrogate representation of the original microstructure space. The samples from this surrogate space need to be mapped to the original space for this technique to be practical. Uncertainty quantification of the microstructure properties driven by the given microstructure realizations then becomes feasible.

In an earlier work [37], we developed a linear embedding methodology to model the topological variations of composite microstructures satisfying some experimentally determined statistical correlations. A model reduction scheme based on principal component analysis (PCA) was developed. This model was successful in reducing the representation of two-phase isotropic microstructures. However, most of the data sets contain essential non-linear structures that cannot be effectively captured by linear model reduction. To this end, a non-linear dimensionality reduction (NLDR) strategy was proposed in [10] to embed data variations into a low-dimensional manifold that serves as the input model for subsequent analysis. Further, the methodology was applied to construct a reduced-order model of a two-phase microstructure and subsequently utilized as a stochastic input model to study the effects of microstructure uncertainty on thermal diffusion. This "manifold learning" method was extended to polycrystals in [8,9], where variability of mechanical response and thermal properties due to topological and orientational uncertainties was examined. This method does not provide a robust mathematical parametric input model which reveals the inherent patterns. In addition, the mapping between the original and the surrogate space is based on the IsoMap [38] algorithm requiring computation of the geodesic distance matrix among data. In general, this matrix may not be well defined and the computation of the matrix could be expensive.

Kernel principal component analysis (KPCA), which first non-linearly maps the input to a "feature" space (the "feature" here refers to a non-linear mapping which is different from the features that are used to describe a microstructure) and then performs PCA (see Fig. 3), is therefore introduced to resolve the issues affiliated with linear PCA and manifold learning model reduction. Successful application of KPCA to modeling of random permeability field of complex geological channelized structures was provided in [39]. In this work, we introduce it for model reduction of the homogenized superalloy polycrystalline microstructure. The microstructures are described by the size and orientation attributes of all constituent grains. A set of grain size and orientation samples are given as the initial input. These samples are generated by simulation. It is assumed that they are obtained through certain random deformation processes and therefore satisfy some statistical constraints. We fix the number of grains to be 54 and the total volume of the microstructure to be 10^{-3} mm^3. Therefore, the mean grain size is fixed. The initial grain size samples are generated according to a lognormal distribution and the orientations are generated from a sequence of random deformation processes that will be introduced in Section 6. After that, we will perform model reduction solely on the sample data assuming that no other

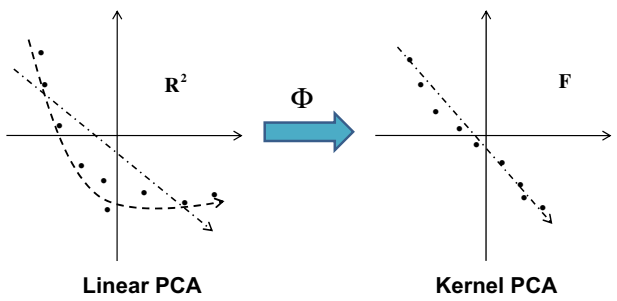

Fig. 3. Basic idea of KPCA. Left: In this non-Gaussian case, the linear PCA cannot effectively capture the non-linear relationship among the realizations in the original space. Right: After the non-linear mapping Φ, realizations become linearly related in the feature space F. Linear PCA can now be performed in F.

information is known (no information about what distribution the grain size follows and what are the random variables controlling the process to generate random textures). The algorithm of PCA/KPCA is summarized below. More details of the mathematical formulation can be found in [30,39,40].

2.2.1. Microstructure model reduction using KPCA

Define a complete probability space $(\Omega, \mathscr{F}, \mathscr{P})$ with sample space Ω, which corresponds to all microstructures resulted from certain random process, $\mathscr{F} \subset 2^{\Omega}$ is the σ-algebra of subsets in Ω and $\mathscr{P} : \mathscr{F} \to [0,1]$ is the probability measure. Each sample $\omega \in \Omega$ is a continuum field representing a microstructure that can be described by a discretized representation, $\mathbf{y} = (y_1, \ldots, y_M)^T : \Omega \to \mathbb{R}^M$. M can be regarded as the number of features in a microstructure. So each y_i, $i = 1, \ldots, M$ is a random variable. The dimensionality of the stochastic input is then the length of the vector $\mathbf{y}$. Any microstructure-sensitive property $\mathscr{A}$ is a function of the microstructure features: $\mathscr{A} = \mathscr{A}(\mathbf{y})$. Therefore, $\mathscr{A}$ is also random. To investigate the variability of $\mathscr{A}$ for microstructures in Ω, we need to be able to compute properties of any sample in Ω. However, only a finite number of realizations $\{\mathbf{y}_1, \ldots, \mathbf{y}_N\}$ of Ω are available. How to explore the space Ω based on a finite number of given microstructure realizations (input data) becomes essential.

The dimensionality of the input, M, is often large. We need to find a reduced order representation of the random field that is consistent with the given data in some statistical sense. To be specific, we want to find a form $\mathbf{y} = f(\xi)$, where ξ, of dimension much smaller than the original input stochastic dimension M, are a set of independent random variables with a specific distribution. Therefore, by drawing samples ξ, we can obtain realizations of the underlying random field, namely, full feature descriptions of microstructures. *KPCA*/*PCA* is used for this purpose.

Given N realizations $\{\mathbf{y}_1, \ldots, \mathbf{y}_N\}$ of a random field $\mathbf{Y}(\omega)$, where each realization is represented as a M-dimensional vector $\mathbf{y}_i \in \mathbb{R}^M$ (e.g. $\mathbf{y}_i$ is a feature realization representing a microstructure by grain size and/or texture), we can map them into a "feature" space $F_i = \Phi(\mathbf{y}_i)$, $i = 1, \ldots, N$. Notice that this "feature" space is in the context of KPCA terminology and different from the microstructure feature input. We will refer the initial microstructure feature input space as the physical space. If $\Phi(\mathbf{y}) = \mathbf{y}$, KPCA is identical to linear PCA. The centered map $\tilde{\Phi}$ is:

$$\tilde{\Phi} = \Phi(\mathbf{y}) - \bar{\Phi}, \tag{2}$$

where $\bar{\Phi} = \frac{1}{N}\sum_{i=1}^{N} \Phi(\mathbf{y}_i)$ is the mean of the Φ-mapped data. The covariance matrix $\mathbf{C}$ in the F space is then

$$\mathbf{C} = \frac{1}{N}\sum_{i=1}^{N} \tilde{\Phi}(\mathbf{y}_i)\tilde{\Phi}^T(\mathbf{y}_i). \tag{3}$$

The dimension of this matrix is $N_F \times N_F$, where N_F is the dimension of the "feature" space.

A kernel eigenvalue problem is formulated which uses only dot products of vectors in the "feature" space. We first substitute the covariance matrix into the l.h.s. of the eigenvalue problem

$$\mathbf{CV} = \lambda \mathbf{V}, \tag{4}$$

to obtain

$$\mathbf{CV} = \frac{1}{N}\sum_{i=1}^{N} \Big(\tilde{\Phi}(\mathbf{y}_i) \cdot \mathbf{V}\Big)\tilde{\Phi}(\mathbf{y}_i), \tag{5}$$

which implies that all solutions $\mathbf{V}$ with $\lambda \neq 0$ lie in the span of $\tilde{\Phi}(\mathbf{y}_1), \ldots, \tilde{\Phi}(\mathbf{y}_N)$. Projecting $\mathbf{V}$ onto sample realizations

$$\mathbf{V} = \sum_{j=1}^{N} \alpha_j \tilde{\Phi}(\mathbf{y}_j), \tag{6}$$

and multiplying Eq. (4) with $\tilde{\Phi}(\mathbf{y}_i)$ from the left, we obtain

$$\frac{1}{N}\sum_{j=1}^{N} \alpha_j \sum_{k=1}^{N} \Big(\tilde{\Phi}(\mathbf{y}_i) \cdot \tilde{\Phi}(\mathbf{y}_k)\Big)\Big(\tilde{\Phi}(\mathbf{y}_k) \cdot \tilde{\Phi}(\mathbf{y}_j)\Big) = \lambda \sum_{j=1}^{N} \alpha_j \Big(\tilde{\Phi}(\mathbf{y}_i) \cdot \tilde{\Phi}(\mathbf{y}_j)\Big), \tag{7}$$

for $i = 1, \ldots, N$. Note here that the vector $\boldsymbol{\alpha}$ is not normalized. Defining the $N \times N$ kernel matrix $\mathbf{K}$ as the dot product of vectors in the "feature" space F:

$$\mathbf{K} : K_{ij} = \big(\Phi(\mathbf{y}_i) \cdot \Phi(\mathbf{y}_j)\big), \tag{8}$$

the corresponding centered kernel matrix is then:

$$\tilde{\mathbf{K}} = \Big(\tilde{\Phi}(\mathbf{y}_i) \cdot \tilde{\Phi}(\mathbf{y}_j)\Big) = \mathbf{HKH}. \tag{9}$$

In the centering matrix $\mathbf{H} = \mathbf{I} - \frac{1}{N}\mathbf{1}\mathbf{1}^T$, $\mathbf{I}$ is the $N \times N$ identity matrix and $\mathbf{1} = [11\ldots1]^T$ is a $N \times 1$ vector. Substituting Eqs. (8) and (9) into Eq. (7), we arrive at the following kernel eigenvalue problem:

$$N\lambda\boldsymbol{\alpha} = \tilde{\mathbf{K}}\boldsymbol{\alpha}, \tag{10}$$

where $\boldsymbol{\alpha} = [\alpha_1, \ldots, \alpha_N]^T$. In the following, for simplicity, we will denote λ_i as the eigenvalues of $\tilde{\mathbf{K}}$, i.e. the solutions $N\lambda_i$ in Eq. (10). We rewrite Eq. (10) in the following matrix form:

$$\tilde{\mathbf{K}}\mathbf{U} = \boldsymbol{\Lambda}\mathbf{U}, \tag{11}$$

where, $\boldsymbol{\Lambda} = \mathrm{diag}\,(\lambda_1, \ldots, \lambda_N)$ and $\mathbf{U} = [\boldsymbol{\alpha}_1, \ldots, \boldsymbol{\alpha}_N]$ is the matrix containing the eigenvectors of the kernel matrix $\tilde{\mathbf{K}}$, where column i is the ith eigenvector $\boldsymbol{\alpha}_i = [\alpha_{i1}, \ldots, \alpha_{iN}]^T$.

Therefore, through Eq. (6), the ith eigenvector of the covariance matrix $\mathbf{C}$ in the feature space can be shown to be [30,40]

$$\mathbf{V}_i = \sum_{j=1}^{N} \alpha_{ij}\tilde{\Phi}(\mathbf{y}_j). \tag{12}$$

Furthermore, the eigenvector $\mathbf{V}_i$ can be normalized. Since the eigenvectors $\boldsymbol{\alpha}_i$ from the eigenvalue problem Eq. (11) are already normalized, the ith orthornormal eigenvector of the covariance matrix $\mathbf{C}$ can be shown to be [30,40]

$$\tilde{\mathbf{V}}_i = \sum_{j=1}^{N} \tilde{\alpha}_{ij}\tilde{\Phi}(\mathbf{y}_j), \quad \text{where } \tilde{\alpha}_{ij} = \frac{\alpha_{ij}}{\sqrt{\lambda_i}}. \tag{13}$$

Let $\mathbf{y}$ be a realization of the random field, with a mapping $\Phi(\mathbf{y})$ in F. According to the theory of linear PCA, $\Phi(\mathbf{y})$ can be decomposed in the following way:

$$\Phi(\mathbf{y}) = \sum_{i=1}^{N} z_i \tilde{\mathbf{V}}_i + \bar{\Phi}, \tag{14}$$

where z_i is the projection coefficient onto the ith eigenvector $\tilde{\mathbf{V}}_i$:

$$z_i = \tilde{\mathbf{V}}_i \cdot \tilde{\Phi}(\mathbf{y}) = \sum_{j=1}^{N} \tilde{\alpha}_{ij}\Big(\tilde{\Phi}(\mathbf{y}) \cdot \tilde{\Phi}(\mathbf{y}_j)\Big). \tag{15}$$

From Eq. (8), it is seen that in order to compute the kernel matrix, only the dot products of vectors in the feature space F are required, while the explicit calculation of the map $\Phi(\mathbf{y})$ does not need to be known. As shown in [30], the dot product can be computed through the use of the kernel function. This is the so called "kernel trick". The kernel function $k(\mathbf{y}_i, \mathbf{y}_j)$ calculates the dot product in space F directly from the vectors of the input space $\mathbb{R}^M$:

$$k(\mathbf{y}_i, \mathbf{y}_j) = \big(\Phi(\mathbf{y}_i) \cdot \Phi(\mathbf{y}_j)\big). \tag{16}$$

The commonly used kernel functions are polynomial kernel and Gaussian kernel.

We can write all the z_i's in a vector form $\mathbf{Z} := [z_1, \ldots, z_N]^T$:

$$\mathbf{Z} = \mathbf{A}^T \mathbf{k}_{\mathbf{y}} + \mathbf{b}, \tag{17}$$

where $\mathbf{A} = \mathbf{H}\widetilde{\mathbf{U}}$, $\mathbf{b} = -\frac{1}{N}\widetilde{\mathbf{U}}^T \mathbf{H}\mathbf{K}\mathbf{1}$ and $\widetilde{\mathbf{U}} = [\tilde{\boldsymbol{\alpha}}_1, \ldots, \tilde{\boldsymbol{\alpha}}_N]$ with $\tilde{\boldsymbol{\alpha}}_i := [\tilde{\alpha}_{i1}, \ldots, \tilde{\alpha}_{iN}]^T$ and

$$\mathbf{k}_{\mathbf{y}} = [k(\mathbf{y}, \mathbf{y}_1), \ldots, k(\mathbf{y}, \mathbf{y}_N)]^T. \tag{18}$$

Suppose the eigenvectors are ordered by decreasing eigenvalues and we only work in the low-dimensional subspace which is spanned by the first r eigenvectors. Then the decomposition in Eq. (14) can be truncated after the first r terms:

$$\Phi(\mathbf{y}) \approx \sum_{i=1}^{r} z_i \mathbf{V}_i + \bar{\Phi} = \sum_{i=1}^{N} \beta_i \Phi(\mathbf{y}_i), \tag{19}$$

where $\boldsymbol{\beta} = \mathbf{A}_r \mathbf{Z}_r + \frac{1}{N}\mathbf{1}$ and β_i is its ith component. Since only the first r eigenvectors are used, $\widetilde{\mathbf{U}}_r = [\tilde{\boldsymbol{\alpha}}_1, \ldots, \tilde{\boldsymbol{\alpha}}_r]$. $\mathbf{A}_r = \mathbf{H}\widetilde{\mathbf{U}}_r$ is a matrix of size $N \times r$ and $\mathbf{Z}_r = [z_1, \ldots, z_r]^T$is a r-dimensional column vector. Details on the derivations of these equations can be found in [39].

Thus, given N samples from the original stochastic feature space F, we can find an approximate r-dimensional subspace $\widetilde{F}$ of F which is spanned by the orthornormal basis $\widetilde{\mathbf{V}}_i$, $i = 1, \ldots, r$. Similar to K–L expansion, the expansion coefficients $\mathbf{Z}_r$ are a r-dimensional random vector that defines this subspace. By drawing samples of $\mathbf{Z}_r$ from it, we can obtain different realizations of $\Phi(\mathbf{y})$ through Eq. (19). The stochastic reduced-order input model in the "feature" space can be defined as: for any realization $\mathbf{Y} \in \widetilde{F}$, we have

$$\mathbf{Y}_r = \sum_{i=1}^{N} \beta_i \Phi(\mathbf{y}_i) = \boldsymbol{\Phi}\boldsymbol{\beta}, \quad \text{with } \boldsymbol{\beta} = \mathbf{A}\boldsymbol{\xi} + \frac{1}{N}\mathbf{1}. \tag{20}$$

Here, $\boldsymbol{\Phi} = [\Phi(\mathbf{y}_1), \ldots, \Phi(\mathbf{y}_N)]$ is a matrix of size $N_F \times N$. The subscript r emphasizes that the realization $\mathbf{Y}_r$ is reconstructed using only the first r eigenvectors. $\boldsymbol{\xi} := [\xi_i, \ldots, \xi_r]^T$is a r-dimensional random vector. If the probability distribution of $\boldsymbol{\xi}$ is known, we can then sample $\boldsymbol{\xi}$ and obtain samples of the random filed in $\widetilde{F}$.

However, the probability distribution of ξ_i is not known to us. What we know is only the realizations of these random coefficients ξ_i, which can be obtained through Eq. (17) by using the available samples:

$$\boldsymbol{\xi}^{(i)} = \mathbf{A}^T \mathbf{k}_{\mathbf{y}_i} + \mathbf{b}, \quad i = 1, \ldots, N. \tag{21}$$

Our problem then reduces to identify the probability distribution of the random vector $\boldsymbol{\xi} := [\xi_i, \ldots, \xi_r]^T$, given its N samples $\boldsymbol{\xi}^{(i)} = \left[\xi_1^{(i)}, \ldots, \xi_r^{(i)}\right]$, $i = 1, \ldots, N$. A polynomial chaos representation is introduced in the next section for representing each component of the random vector $\boldsymbol{\xi}$ in terms of another random vector with known distribution.

Finally, according to the properties of the K–L expansion [4,5,41] used in the "feature" space, the random vector $\boldsymbol{\xi}$ satisfies the following two conditions:

$$E[\xi_i] = 0, \quad E[\xi_i \xi_j] = \delta_{ij}\frac{\lambda_i}{N}, \quad i,j = 1, \ldots, r. \tag{22}$$

Therefore, the random coefficients ξ_i are uncorrelated but not independent.

By sampling $\boldsymbol{\xi}$, we can reconstruct high-dimensional Φ-mapped features in F space. By applying an appropriate "pre-image" scheme [40], realizations in the original physical space (namely, microstructures) can be obtained. A weighted K-nearest neighbor (KNN) pre-imaging algorithm has been designed in [10,39] and will be adopted in this work (Section 4) for KPCA microstructure reconstruction, while for PCA, the pre-imaging is directly performed through Eq. (20) as $\Phi(\mathbf{y}) = \mathbf{y}$.

In practice, the form of map $\Phi(\mathbf{y})$ is not known nor required. Only the kernel function (dot product in the F space) $k(\mathbf{y}_i, \mathbf{y}_j)$ is needed. For linear PCA, the kernel function is simply the dot product in the input space (1st order polynomial)

$$k(\mathbf{y}_i, \mathbf{y}_j) = (\mathbf{y}_i \cdot \mathbf{y}_j), \tag{23}$$

implying that $\Phi(\mathbf{y}) = \mathbf{y}$; and for KPCA, various kernels may be chosen. A commonly selected one is the Gaussian kernel (or radial basis function (RBF)):

$$k(\mathbf{y}_i, \mathbf{y}_j) = \exp\left(-\frac{\|\mathbf{y}_i - \mathbf{y}_j\|^2}{2\sigma^2}\right), \tag{24}$$

where $\|\mathbf{y}_i - \mathbf{y}_j\|^2$ is the squared L_2-distance between two realizations. The kernel width parameter σ is computed using the average minimum distance between two realizations in the input space [42]:

$$\sigma^2 = c\frac{1}{N}\sum_{i=1}^{N} \min_{j \neq i} \|\mathbf{y}_i - \mathbf{y}_j\|^2, \; j = 1, \ldots, N, \tag{25}$$

where c is a user-controlled parameter.

3. Polynomial chaos expansion of stochastic reduced-order model

As explained in the last section, we need to draw samples $\boldsymbol{\xi}$ from the reduced space and reconstruct microstructure realizations in order to investigate material property variability of microstructures. To this end, the reduced surrogate space needs to be constructed and mapped to an appropriate distribution in which sampling is convenient. Polynomial chaos expansion (PCE) [5,32,33] is therefore introduced to represent $\boldsymbol{\xi}$ as a function of Gaussian or uniform random variables $\boldsymbol{\eta}$. As mentioned before, the components of $\boldsymbol{\xi}$ are uncorrelated but not necessarily independent. Although Rosenblatt transformation [43] can be used to decompose the problem to a set of independent random variables, this is computationally expensive for high-dimensional problems. In this work, we assume the independence between the components of $\boldsymbol{\xi}$. It has been shown in various applications [41,44] that this assumption gives rather accurate results.

Following the independence assumption of ξ_i, each of them can be expanded onto a one-dimensional polynomial chaos (PC) basis of degree p:

$$\xi_i = \sum_{j=0}^{p} \gamma_{ij} \Psi_j(\eta_i), \quad i = 1, \ldots, r, \tag{26}$$

where the η_i are i.i.d. random variables. The random basis functions $\{\Psi_j\}$ are chosen according to the type of random variable $\{\eta_i\}$ that has been used to describe the random input. For example, if Gaussian random variables are chosen then the Askey based orthogonal polynomials $\{\Psi_j\}$ are chosen to be Hermite polynomials; if η_i are chosen to be uniform random variables, then $\{\Psi_j\}$ must be Legendre polynomials [32].

Gaussian–Hermite and Uniform-Legendre formats will be considered for the reconstruction of reduced-order random variables (see Section 6). The PC coefficients are computed as

$$\gamma_{ij} = \frac{E\left[\xi_i \Psi_j(\eta_i)\right]}{E\left[\Psi_j^2(\eta_i)\right]}. \tag{27}$$

If Gaussian–Hermite chaos is chosen, Eq. (27) can be expressed as

$$\gamma_{ij} = \frac{1}{\sqrt{2\pi j!}} \int_{-\infty}^{+\infty} \xi_i \Psi_j(\eta_i) e^{-\frac{\eta_i^2}{2}} d\eta_i, \tag{28}$$
$$i = 1, \ldots, r, \quad j = 0, \ldots, p.$$

If Uniform-Legendre is chosen, Eq. (27) becomes

$$\gamma_{ij} = \frac{2j+1}{2}\int_{-1}^{1} \xi_i \Psi_j(\eta_i) d\eta_i, \quad i = 1,\ldots,r, \quad j = 0,\ldots,p. \tag{29}$$

A proper method is needed to evaluate these integrals. However, it is noted that the random variable ξ does not belong to the same stochastic space as η, and we only have a number of N realizations of ξ. The distribution of ξ is invisible. A non-linear mapping Γ: $\eta \to \xi$ is thus needed which preserves the probabilities such that $\Gamma(\eta)$ and ξ have the same distributions. A non-intrusive projection based on empirical cumulative distribution functions (CDFs) of samples developed in [41] is utilized to build the map. The integral in Eq. (27) is then computed using Gauss quadrature.

The non-linear mapping Γ: $\eta \to \xi$ can be defined as shown below for each ξ_i:

$$\xi_i \overset{d}{=} \Gamma_i(\eta_i), \quad \Gamma_i \equiv F_{\xi_i}^{-1} \circ F_{\eta_i}, \tag{30}$$

where F_{ξ_i} and F_{η_i} denote the CDFs of ξ_i and η_i, respectively. Here, the equalities, "$\overset{d}{=}$" is interpreted in the sense of distribution such that the probability density functions (PDFs) of random variables on both sides are equal. The marginal CDF of the samples ξ_i can be evaluated numerically from the available data. Kernel density estimation is used to construct the empirical CDF of ξ_i. Let $\left\{\xi_i^{(s)}\right\}_{s=1}^{N}$ be N samples of ξ_i obtained from Eq. (15). The marginal PDF of ξ_i is then:

$$p_{\xi_i}(\xi_i) \approx \frac{1}{N}\sum_{s=1}^{N} \frac{1}{\sqrt{2\pi}\tau} \exp\left(-\frac{\xi_i - \xi_i^{(s)}}{2\tau^2}\right). \tag{31}$$

The marginal CDF of ξ_i is obtained by integrating Eq. (31) and the inverse CDF can be computed.

Having the map Γ_i, the coefficients γ_{ij} are subsequently computed via Gauss quadrature.

After mapping the reduced space to Gaussian or uniform distribution, Monte Carlo or adaptive sparse grid collocation (ASGC) can be used to sample new realizations. Since the sampling space of ASGC is a unit hypercube $[0,1]^h$, we need to further map the independent Gaussian ($\mathcal{N}(0,1)$) or uniform ($\mathcal{U}(-1,1)$) variables to the hypercube based on CDF.

$$\eta_i = \Upsilon_i(v_i), \quad \Upsilon_i = F_{\eta_i}^{-1}, \quad i = 1,\ldots,r, \tag{32}$$

where $v_i \sim \mathcal{U}(0,1)$ is the sample space of the ith component of ASGC, F_{η_i} is the CDF of η_i.

4. The pre-image problem in KPCA

The sampled random variables after reconstruction (Eq. (26)) are reduced-order representations. For linear PCA, the recovery of a microstructure is straightforward using Eq. (20), since $\mathbf{Y} = \Phi(\mathbf{y}) = \mathbf{y}$. For KPCA, the reconstructed reduced-order representations are in the "feature" space F. Through Eq. (20), we can find the high-dimensional representations, but still, in the "feature" space ($\Phi(\mathbf{y}) \neq \mathbf{y}$). However, what we need are the realizations in the physical input space $\mathbb{R}^M$, which requires the inverse mapping $\mathbf{y} = \Phi^{-1}(\mathbf{X})$. Recall that in order to construct the eigenvalue problem in the feature space, the mapping $\mathbf{Y} = \Phi(\mathbf{y})$ is not necessary as long as the kernel function is provided. Therefore, the inverse mapping needs to be constructed approximately. This inverse mapping problem is known as the "pre-imaging" problem. For each realization $\mathbf{Y}$ in the "feature space', it provides an approximation of the corresponding realization in the physical input space, i.e. $\hat{\mathbf{y}} \approx \Phi^{-1}(\mathbf{Y})$.

A weighted K-nearest neighbor scheme is adopted for finding the pre-images. The basic idea is that for an arbitrary realization $\mathbf{Y}$ in F, we can first compute its distances $\tilde{d}_i$, $i = 1,\ldots,K$ to the K-nearest neighbors $\mathbf{Y}_i$, $i = 1, \ldots, K$ in F. Then the distances d_i, $i = 1, \ldots, K$ between its counterpart $\hat{\mathbf{y}}$ and K-nearest neighbors, $\mathbf{y}_i$, $i = 1, \ldots, K$, in the physical space are recovered. The pre-image $\hat{\mathbf{y}}$ is then computed by

$$\hat{\mathbf{y}} = \frac{\sum_{i=1}^{K} \frac{1}{d_i}\mathbf{y}_i}{\sum_{i=1}^{K} \frac{1}{d_i}}. \tag{33}$$

The distance between $\mathbf{Y}$ and $\Phi(\mathbf{y}_i)$ in the feature space is defined as

$$\tilde{d}_i^2(\mathbf{Y}, \Phi(\mathbf{y}_i)) := \|\mathbf{Y} - \Phi(\mathbf{y}_i)\|^2 = \|\mathbf{Y}\|^2 + \|\Phi(\mathbf{y}_i)\|^2 - 2\mathbf{Y}_r^T \Phi(\mathbf{y}_i), \tag{34}$$

for $i = 1, \ldots, N$. Recall that for Gaussian kernel, $k(\mathbf{y}_i,\mathbf{y}_i) = 1$ and $\mathbf{Y} = \sum_{i=1}^{N} \beta_i \Phi(\mathbf{y}_i)$. N is the total number of the given data (microstructure realizations). Then each feature distance $\tilde{d}_i^2(\mathbf{Y}, \Phi(\mathbf{y}_i))$, $i = 1,\ldots,N$ can be computed in the following matrix form [39]:

$$\tilde{d}_i^2 = 1 + \boldsymbol{\beta}^T \mathbf{K} \boldsymbol{\beta} - 2\boldsymbol{\beta}^T \mathbf{k}_{\mathbf{y}_i}, \tag{35}$$

for $i = 1, \ldots, N$.

Denote the vector $\tilde{\mathbf{d}}^2 = [\tilde{d}_1^2, \ldots, \tilde{d}_N^2]^T$ and we can sort this vector in ascending order to identify the K-nearest neighbors of $\mathbf{Y}$ from $\Phi(\tilde{\mathbf{y}}_i)$, $i = 1, \ldots, n$.

On the other hand, the squared feature distance between the Φ-map of the pre-image $\hat{\mathbf{y}}$ and $\Phi(\mathbf{y}_i)$ is given as:

$$\begin{aligned} \tilde{d}_i^2(\Phi(\hat{\mathbf{y}}), \Phi(\mathbf{y}_i)) &= \|\Phi(\hat{\mathbf{y}}) - \Phi(\mathbf{y}_i)\|^2 \\ &= k(\hat{\mathbf{y}}, \hat{\mathbf{y}}) + k(\mathbf{y}_i, \mathbf{y}_i) - 2k(\hat{\mathbf{y}}, \mathbf{y}_j) \\ &= 2(1 - k(\hat{\mathbf{y}}, \mathbf{y}_i)), \end{aligned} \tag{36}$$

for $i = 1, \ldots, N$. Note that in the derivation above, we used that $k(\hat{\mathbf{y}}, \hat{\mathbf{y}}) = k(\mathbf{y}_i, \mathbf{y}_i) = 1$ for a Gaussian kernel. Furthermore, the squared input-space distance can be computed from the following equation:

$$k(\hat{\mathbf{y}}, \mathbf{y}_i) = \exp\left(-\frac{\|\hat{\mathbf{y}} - \mathbf{y}_i\|^2}{2\sigma^2}\right),$$

from which we obtain

$$d_i^2 = \|\hat{\mathbf{y}} - \mathbf{y}_i\|^2 = -2\sigma^2 \log(k(\hat{\mathbf{y}}, \mathbf{y}_i)), \tag{37}$$

for $i = 1, \ldots, N$. Substituting the expression of $k(\hat{\mathbf{y}}, \mathbf{y}_j)$ from Eq. (36) into Eq. (37), one arrives at

$$d_i^2 = \|\hat{\mathbf{y}} - \mathbf{y}_i\|^2 = -2\sigma^2 \log\left(1 - 0.5\tilde{d}_i^2\right), \tag{38}$$

for $i = 1, \ldots, N$. Because we try to find an approximate pre-image such that $\Phi(\hat{\mathbf{y}}) \approx \mathbf{Y}$, it is straightforward to identify the relationship $d_i^2 \approx \tilde{d}_i^2$. Therefore, the squared input-distance between the approximate pre-image $\hat{\mathbf{y}}$ and the ith input data realization can be computed by:

$$d_i^2 = \|\hat{\mathbf{y}} - \mathbf{y}_i\|^2 = -2\sigma^2 \log\left(1 - 0.5\tilde{d}_i^2\right), \tag{39}$$

for $i = 1, \ldots, N$ and where $\tilde{d}_i^2$ is given by Eq. (35).

Finally, the pre-image $\hat{\mathbf{y}}$ for a feature space realization $\mathbf{Y}$ is given by Eq. (33). It is noted that here we use the K-nearest neighbors in the "feature" space. However, they are the same as the K-nearest neighbors in the input space since Eq. (39) is monotonically increasing. Therefore, the pre-image $\hat{\mathbf{y}}$ of an arbitrary realization in the "feature" space is the weighted sum of the pre-images of the K-nearest neighbors of $\mathbf{Y}$ in the "feature" space, where the nearest neighbors are taken from the samples $\mathbf{y}_i$, $i = 1, \ldots, N$. A unique pre-image can now be obtained using simple algebraic calculations in a single step (no iteration is required) that is suitable for stochastic simulation.

5. Two-phase crystal plasticity constitutive model

The crystal plasticity constitutive model is critical for predicting the mechanical properties of polycrystalline materials. The previously developed single-phase constitutive model for FCC crystals [45] is here extended to two-phase superalloy, IN 100. In this material, the second phase, γ', disperses in the γ phase in three forms: primary (large particles that may not exist due to insufficient heat treatment), secondary (medium size particles) and tertiary (particles of small size and low volume fraction) precipitates. The strength of the superalloy is significantly reinforced due to the existence of these particles. A homogenized superalloy constitutive model will be adopted to study the polycrystalline microstructure behavior. The second phase configuration is not explicitly modeled. Effects from the second phase are taken into account through particular parameters in the constitutive model. In the homogenized model, we take the effective property of both phases in a single phase medium representation.

Cube slip $\langle 1\,1\,0\rangle\{1\,0\,0\}$ systems are introduced to take cross slip mechanism at high temperatures into consideration. The rate dependent flow rule which estimates the shearing rate on each slip system includes a back force term for the modeling of the Baushinger effect arising principally from matrix dislocation interaction with γ' phase. The effect of volume and size of γ' precipitates on material strength is taken into account by constitutive parameters. The constitutive equations are summarized below and detailed in [25,26,28].

The flow rule of slip system α is

$$\dot{\gamma}^{(\alpha)} = \left[\dot{\gamma}_0^{(\alpha)}\left\langle\frac{|\tau^{(\alpha)}-\chi_\lambda^{(\alpha)}|-\kappa_\lambda^{(\alpha)}}{D_\lambda^{(\alpha)}}\right\rangle^{n_1}\right. \tag{40}$$

$$\left. + \dot{\gamma}_1^{(\alpha)}\left\langle\frac{|\tau^{(\alpha)}-\chi_\lambda^{(\alpha)}|}{D_\lambda^{(\alpha)}}\right\rangle^{n_2}\right]\mathrm{sgn}(\tau^{(\alpha)}-\chi_\lambda^{(\alpha)}), \tag{41}$$

where $\dot{\gamma}_0^{(\alpha)}$ is the initial shearing rate, $D_\lambda^{(\alpha)}$ is the drag stress assumed to be constant. $\lambda = \{\mathrm{oct},\mathrm{cub}\}$ refers to the octahedral and cube slip systems, respectively. The function $\langle x\rangle$ returns x if $x > 0$ and returns 0, otherwise. The resolved shear stress on the α slip system $\tau^{(\alpha)}$ is computed by

$$\tau^{(\alpha)} = \overline{\mathbf{T}} : \left(\mathbf{m}_0^{(\alpha)} \otimes \mathbf{n}_0^{(\alpha)}\right), \tag{42}$$

where $\overline{\mathbf{T}}$ is the PK-II stress and $\mathbf{m}_0^{(\alpha)}$ and $\mathbf{n}_0^{(\alpha)}$ are vectors in the slip direction and normal to the slip plane, respectively, in the original configuration, since a total Lagrangian algorithm is adopted. $\overline{\mathbf{T}}$ is related to local elastic deformation gradient $\mathbf{F}^e$ via the fourth-order stiffness tensor $\mathbf{C}^e$:

$$\overline{\mathbf{T}} = \mathbf{C}^e \cdot \overline{\mathbf{E}} = \frac{\mathbf{1}}{\mathbf{2}}\mathbf{C}^{\mathbf{e}} \cdot (\mathbf{F}^{\mathbf{eT}}\mathbf{F}^{\mathbf{e}} - \mathbf{I}). \tag{43}$$

The evolution of the slip resistance $\kappa_\lambda^{(\alpha)}(\lambda = \mathrm{cub},\mathrm{oct})$ follows the Taylor strain hardening law determined by dislocation density $\rho_\lambda^{(\alpha)}$:

$$\kappa_\lambda^{(\alpha)} = \kappa_{0,\lambda}^{(\alpha)} + \alpha_t \mu_{mix} b\sqrt{\rho_\lambda^{(\alpha)}}, \tag{44}$$

where $\alpha_t = \langle 0.1 - 0.68 f'_{p1} + 1.1 f'^2_{p1}\rangle$, $\mu_{mix} = (f_{p1}+f_{p2}+f_p3)\mu_{\gamma'} + f_m\mu_\gamma$. $\mu_{\gamma'}$ and μ_γ are shear moduli for γ' precipitates and γ matrix, respectively. The magnitude of Burgers vector is $b = (f_{p1}+f_{p2}+f_{p3})b_{\gamma'} + f_m b_\gamma$. f_{p1}, f_{p2}, f_{p3} are volume fractions of primary, secondary, and tertiary γ' precipitates, respectively, and $f_m = 1 - f_{p1} - f_{p2} - f_{p3}$ is the volume fraction of γ matrix phase. $f'_{p1} = \frac{f_{p1}}{f_{p1}+f_m}$, $f_{p2} = \frac{f_{p2}}{f_{p2}+f_m}$ and $f_{p3} = \frac{f_{p3}}{f_{p3}+f_m}$. For different slip systems, the initial slip resistance can be evaluated by

$$\kappa_{0,oct}^{(\alpha)} = \left[\left(\tau_{0,oct}^{(\alpha)}\right)^{n_k} + \psi_{oct}^{n_k}\right]^{1/n_k} + (f_{p1}+f_{p2})\tau_{ns}^{(\alpha)},$$
$$\kappa_{0,cub}^{(\alpha)} = \left[\left(\tau_{0,cub}^{(\alpha)}\right)^{n_k} + \psi_{cub}^{n_k}\right]^{1/n_k}, \tag{45}$$

where

$$\psi_\lambda = c_{p1}\sqrt{w\frac{f'_{p1}}{d_1}} + c_{p2}\sqrt{w\frac{f'_{p2}}{d_2}} + c_{p3}\sqrt{wf'_{p3}d_3} + c_{gr}d_{gr}^{-0.5}, \quad w = \frac{\Gamma_{APB}}{\Gamma_{APB-ref}}, \tag{46}$$

and

$$\tau_{ns}^{(\alpha)} = h_{pe}\tau_{pe}^{(\alpha)} + h_{cb}|\tau_{cb}^{(\alpha)}| + h_{se}\tau_{se}^{(\alpha)}, \tag{47}$$

in which Γ_{APB} is the anti-phase boundary energy density here taken be equal to $\Gamma_{APB-ref}$, d_i, $i = 1, 2, 3$ are the sizes of precipitates, and d_{gr} is the grain size.

The dislocation density evolution has the following form:

$$\dot{\rho}_\lambda^{(\alpha)} = h_0\left\{Z_0 + k_{1,\lambda}\sqrt{\rho_\lambda^{(\alpha)}} - k_{2,\lambda}\rho_\lambda^{(\alpha)}\right\}|\dot{\gamma}^{(\alpha)}|, \quad Z_0 = \frac{k_\delta}{bd_{\delta eff}}, \quad d_{\delta eff} \approx \left(\frac{2}{d_{2\delta}}\right)^{-1}. \tag{48}$$

The evolution of the back stress $\chi_\lambda^{(\alpha)}$ is also based on dislocation density and shear rate:

$$\dot{\chi}_\lambda^{(\alpha)} = C_\chi\left\{\eta\mu_{mix}b\sqrt{\rho_\lambda^{(\alpha)}}\,\mathrm{sgn}\left(\tau^{(\alpha)} - \chi_\lambda^{(\alpha)}\right) - \chi_\lambda^{(\alpha)}\right\}|\dot{\gamma}^{(\alpha)}|, \tag{49}$$

$$\eta = \frac{\eta_{0,\lambda}Z_0}{Z_0 + k_{1,\lambda}\sqrt{\rho_\lambda^{(\alpha)}}},$$

where $C_\chi = 123.93 - 433.98 f'_{p2} + 384.06 f'^2_{p2}$.

An implicit iterative algorithm is used for the solution of the non-linear constitutive equations. In initial slip resistance $\kappa_{0,\lambda}$, the grain size effect is introduced in the form of the Hall–Petch law $\kappa \propto d_{gr}^{-0.5}$.

The parameters in the constitutive model can be calibrated by experimental results for specific superalloys (e.g. IN 100). In the current work, the same parameters for superalloys at 650°C listed in [25] are adopted. For additional information about the constitutive model refer to [26,27].

Strain based fatigue indicator parameters (FIPs) related to small crack formation and early growth are extracted as the measure of fatigue resistance, or more precisely as a measure of driving forces for fatigue crack formation [24]. The four FIPs of interest are the cumulative plastic strain per cycle (P_{cyc}), which correlates to the crack incubation life; the cumulative net plastic shear strain measure (P_r), which correlates with dislocations pile-up on grain boundaries; the Fatemi–Socie parameter (P_{FS}), which relates to the small crack growth; and the maximum range of cyclic plastic shear strain parameter (P_{mps}) [26]. The definitions of these FIPs are as follows.

The cumulative plastic strain per cycle (P_{cyc}):

$$P_{cyc} = \int_{cyc}\sqrt{\frac{2}{3}}\dot{p}dt = \int_{cyc}\sqrt{\frac{2}{3}\mathbf{D}^p : \mathbf{D}^p}dt, \tag{50}$$

where $\mathbf{D}^p$ is the plastic rate of deformation tensor. The crack incubation life ($N_{Inc.}$) is related to a critical value, p_{crit}, i.e.,

$$P_{cyc}N_{inc} = p_{crit}. \tag{51}$$

The cumulative net plastic shear strain measure (P_r):

$$P_r = \max\left(\int_{cycle}\dot{\epsilon}_{ij}^p n_i m_j dt\right), \tag{52}$$

where $\mathbf{m}$ is the direction along any given plane with normal $\mathbf{n}$. The maximum value of this parameter is obtained along all possible slip directions over all possible planes for one cycle.

The Fatemi–Socie parameter (P_{FS}):

$$P_{FS} = \frac{\Delta\gamma^p_{max}}{2}\left[1 + k^{\star}\frac{\sigma_n^{max}}{\sigma_y}\right], \tag{53}$$

where $\Delta\gamma^p_{max}$ is the maximum range of cyclic plastic shear strain, σ_n^{max} is the peak tensile stress normal to the plane associated with this maximum shear range and σ_y is the cyclic yield strength estimated by the Von-Mises stress at the yield strain ϵ_y. Here, we choose $\epsilon_y = 0.77\%$. The parameter $k^{\star}$ could be a function of several material properties in addition to the multiaxial strain state. In the current work, a constant value $k^{\star} = 0.5$ is used as suggested in [26].

The maximum range of cyclic plastic shear strain parameter (P_{mps}):

$$P_{mps} = \frac{\Delta\gamma^p_{max}}{2}. \tag{54}$$

This parameter is used when the incubation life is completely controlled by the irreversible motion of the dislocations with no assist of normal stress, namely, $k^{\star} = 0$ in Eq. (53).

An example of Nickel-based superalloy microstructure consisting of 54 grains having random orientations in a 10^{-3} mm^3 volume subjected to cyclic loading (tension and compression along z-direction) is demonstrated below. The volume fractions and sizes of γ' precipitates are given by $f_{p1} = 0$, $f_{p2} = 0.42$, $d_2 = 108$ nm, $f_{p3} = 0.11$, $d_3 = 7$ nm. Mechanical behavior of the microstructure is controlled by the constitutive model introduced above. All the FIPs are computed throughout the third deformation loop. The last non-Schmid term $\tau_{ns}^{(\alpha)}$ in $\kappa_{0,oct}^{(\alpha)}$ is assumed to be 0. This is an approximation as its contribution to threshold stress is not insignificant. The stress–strain response of cyclic loading condition with three loops and the normalized distributions of the FIPs are plotted in Fig. 4. Note that the x-axis in both Fig. 4a is true strain, not plastic strain. The maximum FIPs over the entire microstructure are $maxP_{cyc} = 1.51 \times 10^{-2}$, $maxP_r = 1.12 \times 10^{-4}$, $maxP_{FS} = 6.50 \times 10^{-3}$, and $maxP_{mps} = 5.98 \times 10^{-3}$.

It is worth mentioning that the Taylor model is used to control the deformation of the microstructure to allow efficient stochastic simulation to be discussed next. As a result, all grains in the microstructure are subjected to the same deformation at

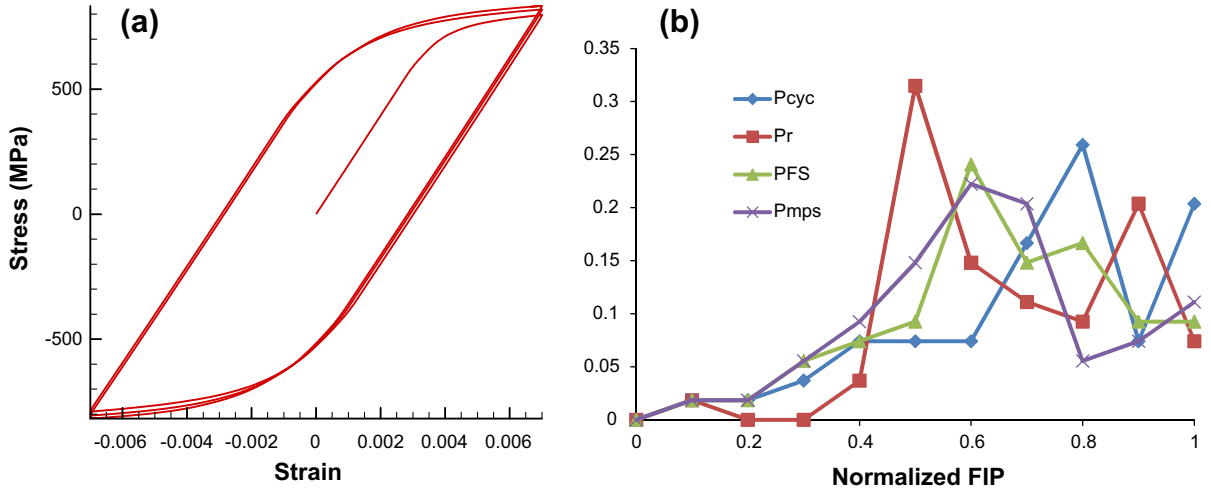

Fig. 4. (a) Stress–strain response during three loops of cyclic loading. The strain rate is 0.001 s^{-1}. (b) Distribution of normalized FIPs at a strain amplitude of $\epsilon = 0.007$.

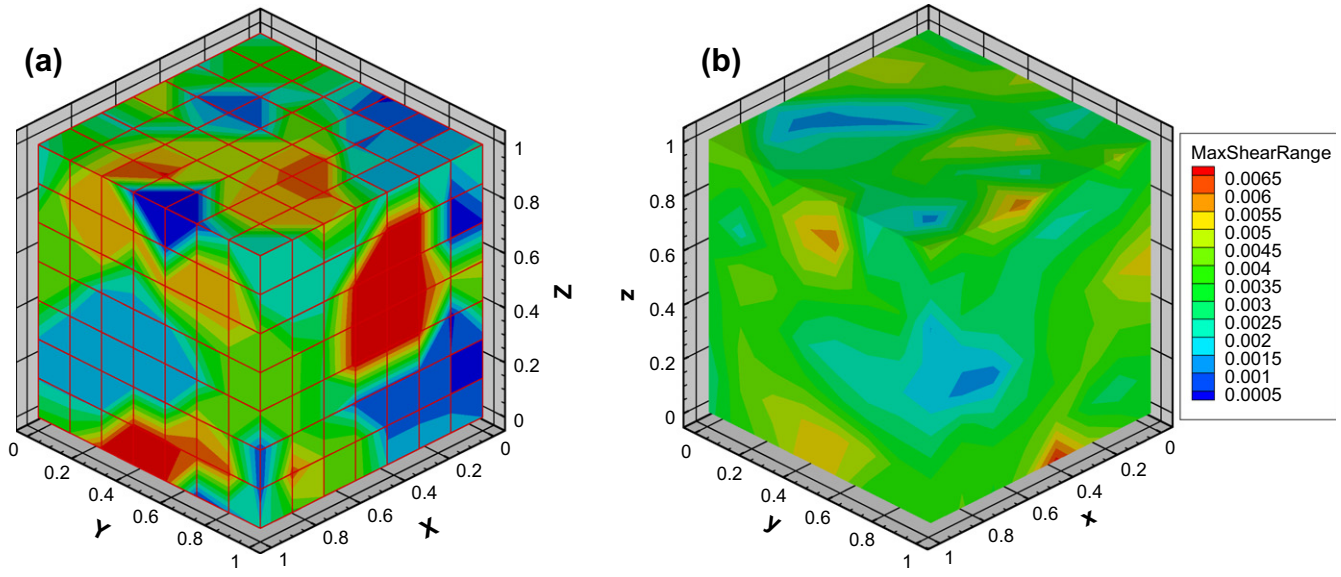

Fig. 5. (a) A 3D finite element realization of polycrystalline microstructure. Each color represents an individual grain. (b) The field of the maximum range of cyclic plastic shear strain parameter at the end of the 3rd loop.

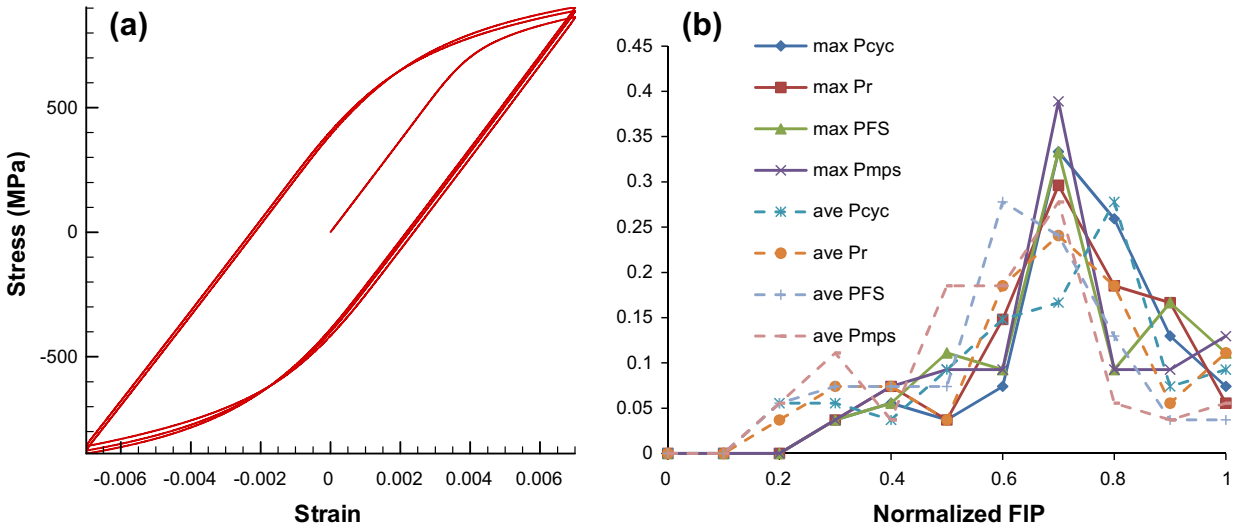

Fig. 6. Finite element simulation results: (a) Stress–strain response during three loops of cyclic loading. (b) Distributions of normalized FIPs at a strain amplitude of $\epsilon = 0.007$.

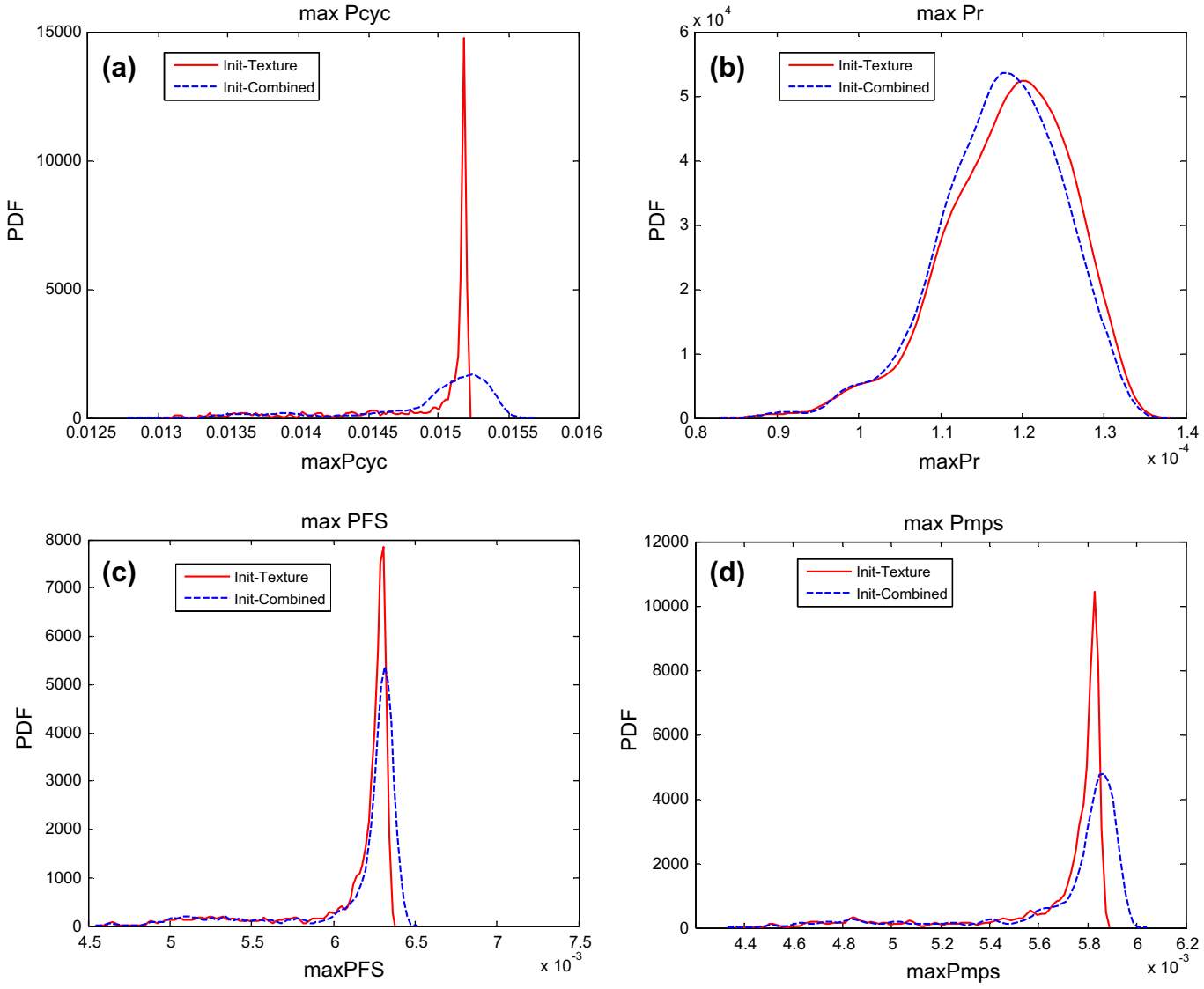

Fig. 7. Distributions of maximum FIPs extracted from the 1000 initial sample microstructures. The solid curves are obtained by considering both grain size and texture features as random sources. The dashed curves are for the case with random texture but with fixed sizes assigned to all grains in the microstructure. (a) *Max* P_{cyc}; (b) *Max* P_r; (c) *Max* P_{FS}; (d) *Max* P_{mps}.

Table 1
Statistics of the maximum FIPs computed from three cases of initial samples: "Texture" means only texture uncertainty is considered; "Grain size" means only that only grain size uncertainty is considered; and "Combined" means that both grain size and texture uncertainties are considered.

	Texture	Grain size	Combined
Max P_{cyc} mean	1.49×10^{-2}	1.50×10^{-2}	1.49×10^{-2}
Max P_{cyc} std	5.02×10^{-4}	2.92×10^{-5}	5.21×10^{-4}
Max P_r mean	1.18×10^{-4}	1.17×10^{-4}	1.17×10^{-4}
Max P_r std	7.53×10^{-6}	6.50×10^{-7}	7.34×10^{-6}
Max P_{FS} mean	6.13×10^{-3}	6.33×10^{-3}	6.15×10^{-3}
Max P_{FS} std	3.41×10^{-4}	1.41×10^{-5}	3.60×10^{-4}
Max P_{mps} mean	5.67×10^{-3}	5.88×10^{-3}	5.70×10^{-3}
Max P_{mps} std	3.03×10^{-4}	6.67×10^{-6}	3.28×10^{-4}

each time step. Heterogeneity of the deformation field due to distinct strength of different grains (induced by grain size, orientation, etc.) is not considered. The distributions of FIPs in the microstructure predicted in this model may not be very accurate but they serve as reasonable fatigue indicators for one grain. We also conducted a 3*D* finite element (FE) analysis on a cubic polycrystalline microstructure with 54 grains (Fig. 5a). The microstructure is discretized using $7 \times 7 \times 7$ brick elements. The maximum and average values of FIPs over all the Gauss points of all elements within an individual grain are evaluated as the representatives of the fatigue driving force of the corresponding grain. The maximum of the grain level FIPs over the entire microstructure are $maxP_{cyc,\ max} = 1.99 \times 10^{-2}$, $maxP_{r,\ max} = 8.16 \times 10^{-4}$, $maxP_{FS,\ max} = 7.90 \times 10^{-3}$, $maxP_{mps,\ max} = 6.76 \times 10^{-3}$, $maxP_{cyc,ave} = 1.49 \times 10^{-2}$, $maxP_{r,ave} = 4.46 \times 10^{-4}$, $maxP_{FS,ave} = 6.21 \times 10^{-3}$, and $maxP_{mps,ave} = 5.44 \times 10^{-4}$. Here, $P_{x,max}/P_{x,ave}$ denotes the maximum/average P_x over all Gauss points within one grain, and $maxP_{x,max}/maxP_{x,ave}$ is the maximum of $P_{x,max}/P_{x,ave}$ over all grains in the microstructure. The contour plot of the maximum range of cyclic plastic shear strain parameter, P_{mps}, is plotted in Fig. 5b.

The true stress–strain curve and normalized distributions of FIPs are demonstrated in Fig. 6. We see that the Taylor simulation gives similar stress–strain response and distributions of FIPs as the FE model. Most of the FIPs obtained from the Taylor model are close to the grain level average FIPs obtained in the FE model. Considering the computational cost that the Taylor model takes only 3 min for one simulation while the FE model takes about 9 h (the efficiency is evaluated here for one processor), we will adopt the Taylor model as the deterministic solver in the further investigation of the variability of FIPs. The fatigue property of a microstructure under cyclic loading can be measured by the maximum FIPs over all grains.

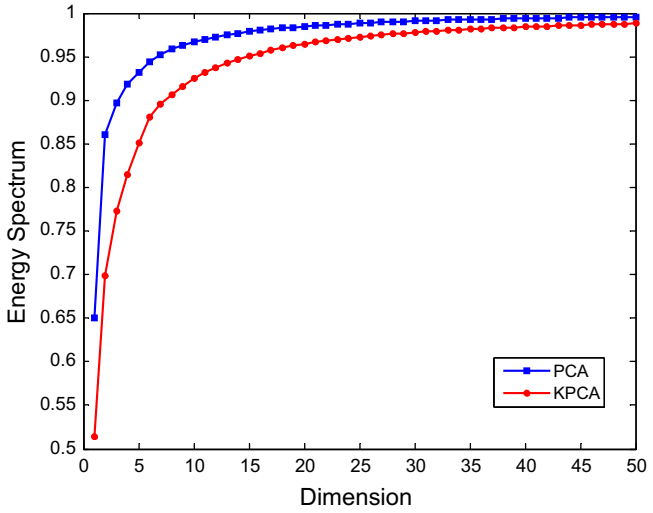

Fig. 9. Plots of the energy spectrum for PCA and KPCA on texture feature. The value of *y*-axis is the total energy proportion captured by the first *x* principal components.

6. Numerical examples

Numerical examples are presented to study the probabilistic distribution of the FIPs of Nickel-based superalloy polycrystalline microstructures using PCA-based model reduction techniques, PC representation and sparse grid collocation method. The deterministic solver adopts the two-phase polycrystal plasticity constitutive model introduced earlier. The maximum FIPs over all grains are used to measure fatigue properties of microstructures. In the following subsections, variability of FIPs due to topological and orientational microstructure uncertainties are examined.

The available information of microstructure features is often given as a limited number of samples that are obtained through a sequence of preprocessing. In the current work, we randomly

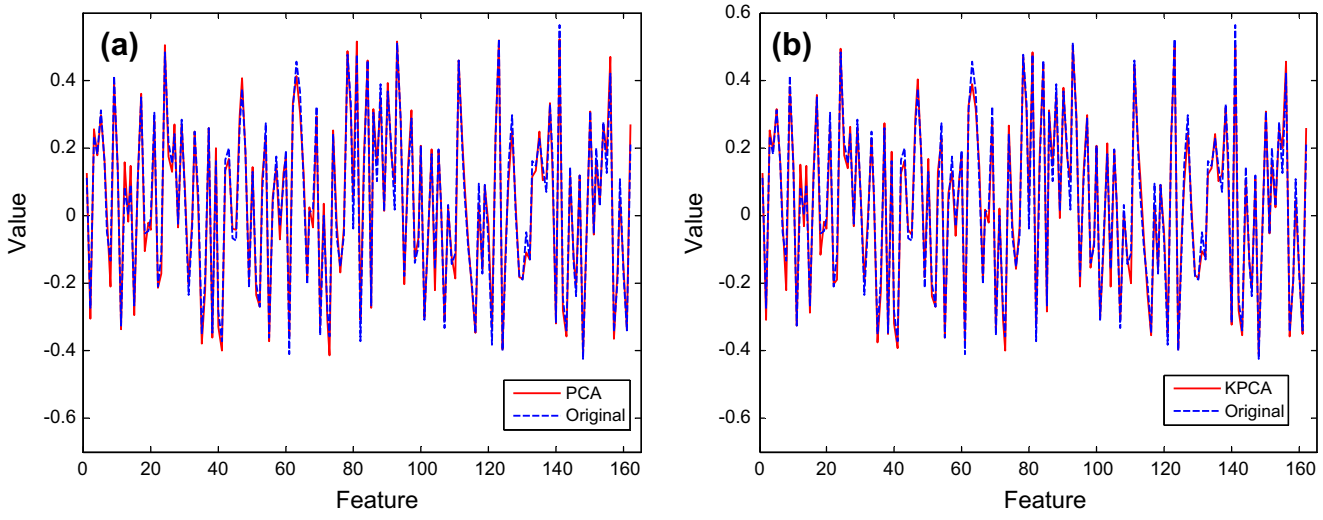

Fig. 8. (a) A PCA reconstructed texture feature compared with the original test sample. The dimensionality of the reduced-order representation is 4, which captures 91.8% of the total "energy". (b) A KPCA reconstructed texture feature compared with the original test sample. The dimensionality of the reduced-order representation is 4, which captures 81.5% of the total "energy".

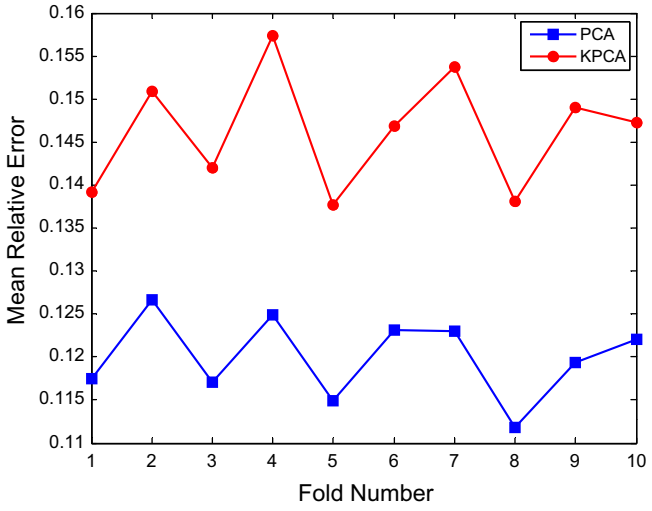

Fig. 10. Averaged relative errors of testing texture samples in 10-fold cross validation for PCA and KPCA.

generate 1000 microstructures through simulation. This operation mimics the industrial random preprocessing and is only for the generation of inherently correlated samples, based on which model reduction would work. After that, the sample data will serve directly as the initial input to the stochastic simulation. The knowledge about how the data was generated will not be known or used in this part of the analysis. Each microstructure is composed of 54 grains in a $V = 1 \times 10^{-3}$ mm^3 domain. The mean grain volume is therefore 1.85×10^{-5} mm^3. By assuming cubic shape of all grains, the mean size is $\langle d_{gr} \rangle = 0.0265$ mm. As indicated in many works, the grain size can be well described by a lognormal distribution. Therefore, we generate grain sizes of a microstructure according to a lognormal distribution defined as

$$p(d_{gr}) = \frac{1}{d_{gr}\sqrt{2\pi\sigma^2}} \exp\left(-\frac{\ln(d_{gr}) - \mu}{2\sigma^2}\right), \tag{55}$$

where d_{gr} is the grain size, and μ, σ refer to the mean and standard deviation of $\ln(d_{gr})$. The mean grain size is $\langle d_{gr} \rangle = \exp(\mu + \sigma^2/2)$, which takes the value 0.0265 mm as mentioned above. The procedure of generating grain size samples is

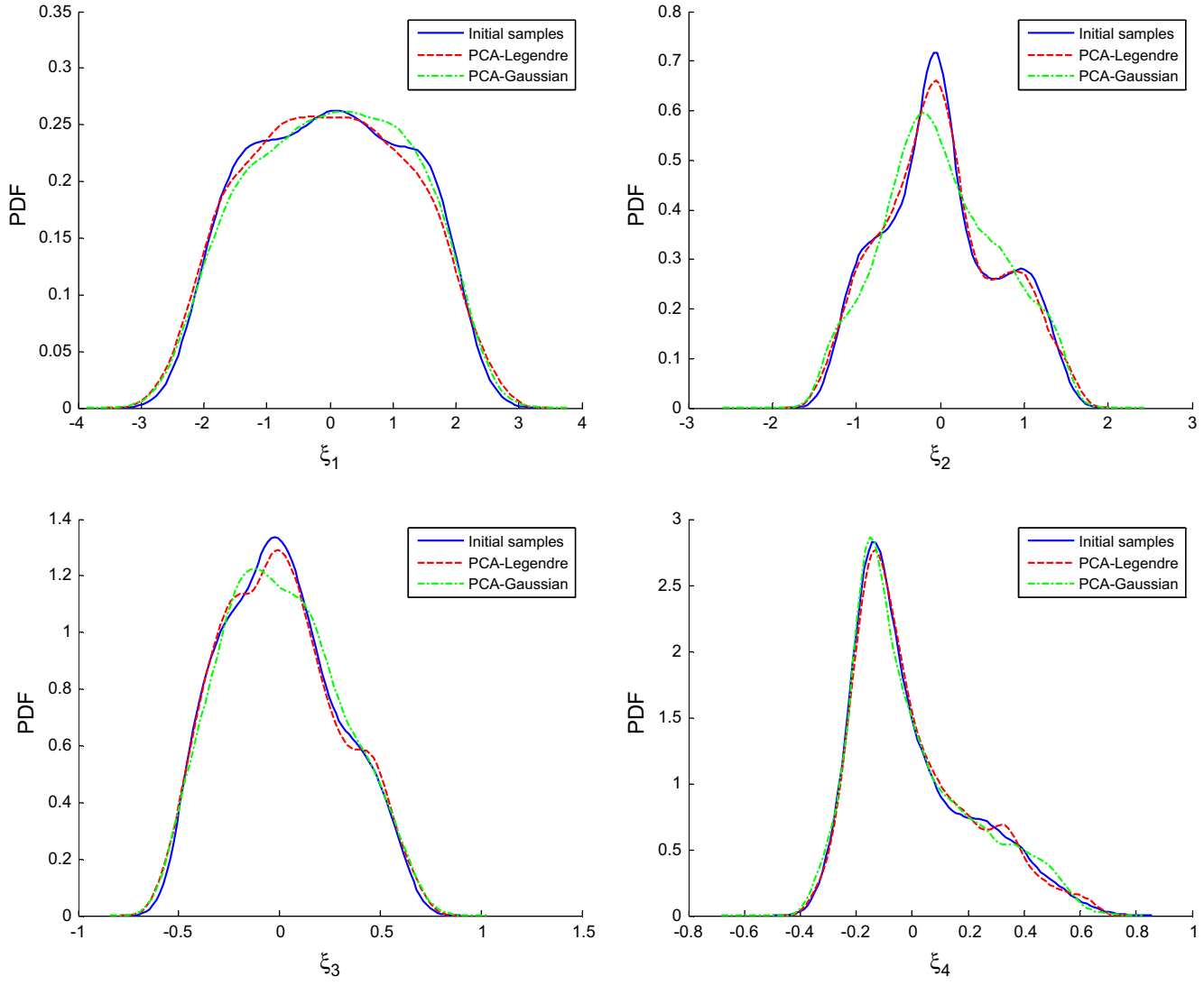

Fig. 11. Marginal PDFs of the initial random variables (the reduced representations obtained after performing PCA on the 1000 given texture samples) and identified random variables obtained using PCE (reconstructed through PCE (Eq. (26)) on 10,000 randomly generated samples from Gaussian or Uniform distribution). The distributions are constructed through kernel density based on data.

as follows. For a single microstructure sample, we first generate 54 approximate grain sizes $\{\hat{d}_{gr,i}, i = 1, \ldots, 54\}$ from the lognormal distribution with $\mu = \ln\langle d_{gr}\rangle - \sigma^2/2$, where $\langle d_{gr}\rangle = 0.0265$ mm and $\sigma = 0.025$. To avoid extreme large or small grains, all grain sizes are constrained within the range $0.4\langle d_{gr}\rangle < \hat{d}_{gr,i} < 2.5\langle d_{gr}\rangle$. If a grain size falls beyond that range, a new one will be generated until it satisfies the inequality. After obtaining all the 54 grain sizes, we will compute the corresponding volumes (cube root) $\widehat{V}_{gr,i} = \hat{d}^3_{gr,i}, i = 1, \ldots, 54$, by assuming spherical grains. Then, the volume fraction $f_{gr,i}$ of each grain i will be obtained after normalization: $f_{gr,i} = \widehat{V}_{gr,i}/\sum_j^{54}\widehat{V}_{gr,j}$. The grain volume $V_{gr,i}$ will be updated by multiplying the volume fraction by the total volume of the microstructure $V = 0.001$ (namely, $V_{gr,i} = V \times f_{gr,i}$, for $i = 1, \ldots, 54$). The grain sizes can be therefore determined by the resultant grain volumes. Repeating this procedure 1000 times, we can obtain 1000 microstructure grain size samples. Assigning an arbitrary texture to all grain size samples and putting them into a sequence of random deformation process, we can derive 1000 random texture that will be collected as the initial texture to the next-step stochastic simulation. To be specific, an arbitrary texture consisted of 54 orientations is firstly assigned to 1000 microstructure samples. Then, these microstructures are input into a sequence of deformation modes controlled by three independent random variables ω_1, ω_2 and ω_3.

$$\mathbf{L} = \omega_1 \begin{bmatrix} 0.5 & 0 & 0 \\ 0 & 0.5 & 0 \\ 0 & 0 & -1 \end{bmatrix} + \omega_2 \begin{bmatrix} 0 & 0 & 0 \\ 0 & 1 & 0 \\ 0 & 0 & -1 \end{bmatrix} + \omega_3 \begin{bmatrix} 0 & -1 & 0 \\ 1 & 0 & 0 \\ 0 & 0 & 0 \end{bmatrix}, \tag{56}$$

where the random variables ω_1, ω_2 and ω_3 determine the deformation rate $\mathbf{L}$ of different modes and vary uniformly from $-0.002\ s^{-1}$ to $0.002\ s^{-1}$. The first mode is compression in the z direction, the second mode is rotation, and the last mode is a shear deformation. At each time step, the deformation of the microstructure is controlled by the combination of these three modes, but for different samples, the combination is different in terms of the deformation rates ω_1, ω_2 and ω_3. At the end of 500 s, the 1000 resultant textures were collected as the input texture database to the stochastic problem. Since our model only updates orientations of grains but leaves their sizes untouched, the resultant microstructures would have the same grain sizes as the input while the texture becomes random. Moreover, the texture evolution is not significantly affected by the

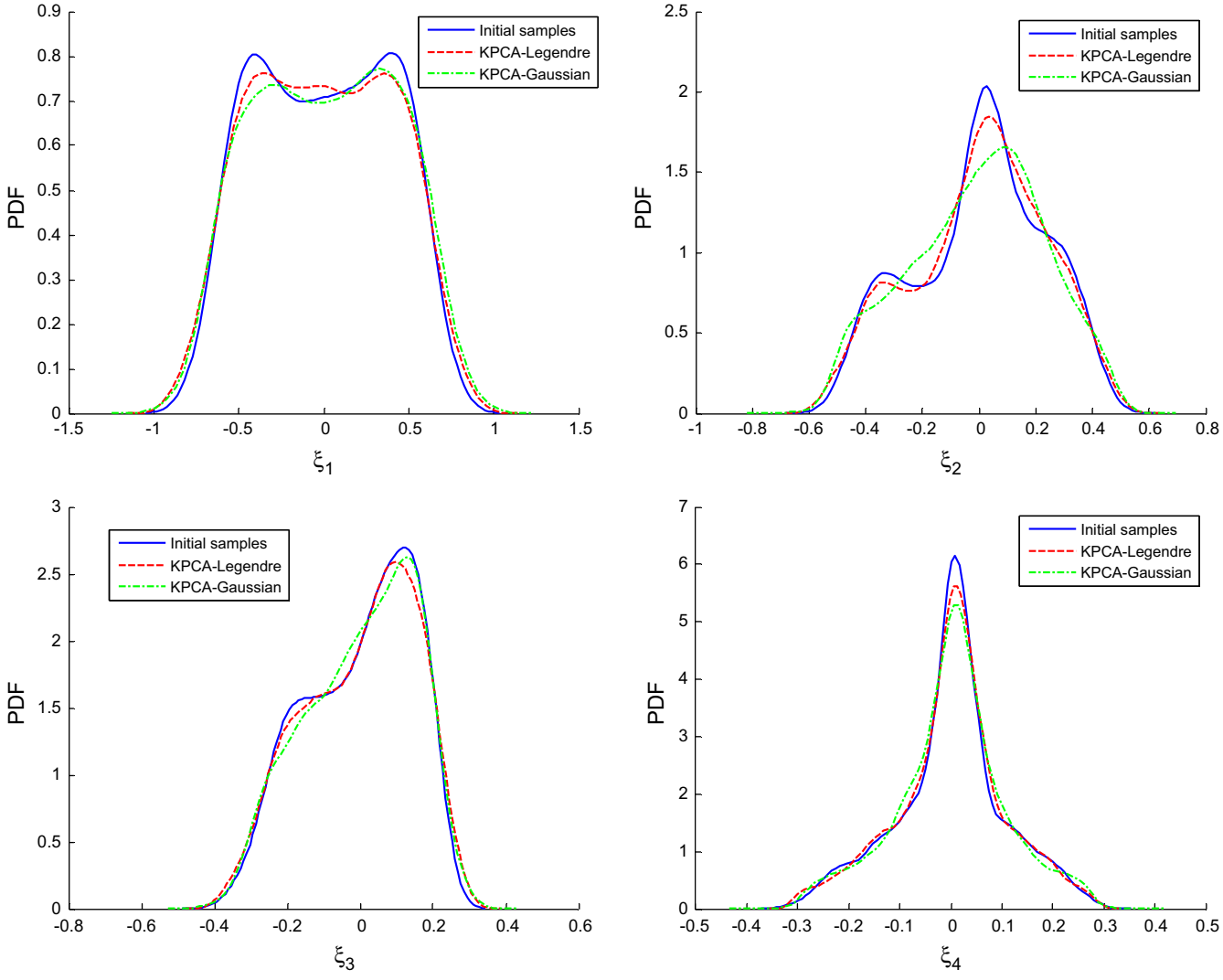

Fig. 12. Marginal PDFs of the initial random variables (the reduced representations obtained after performing KPCA on the 1000 given texture samples) and identified random variables obtained using Hermite or Legendre PCE. The distributions are constructed through kernel density based on data.

grain size according to the constitutive model. Therefore, the correlation of texture and grain size features is quite weak.

After generating the 1000 grain size and texture samples, we take them as the given input data to the following stochastic simulation investigating material properties due to initial microstructure uncertainties. They are the only accessible information, while the knowledge of how they are generated is blind to the uncertainty quantification process. The correlation within the feature samples will be exploited by the construction of correlation matrix through PCA/KPCA model reduction. Inserting random grain size or orientation features to the model reduction, the surrogate microstructure representation is derived. Then, polynomial chaos expansion (PCE) is used to map the reduced-order space to a known distribution, form which samples can be easily drawn and ASGC or/and MC can be conveniently introduced to solve for the variability of FIPs. Distributions and convex hulls and FIPs will be constructed according to the solution. Simulations using different models (i.e. linear/non-linear PCA, Uniform-Legendre/Gaussian–Hermite PCE, ASGC/MC) are conducted and compared. The effect of the selected dimensionality of the reduced space is also studied.

Here, we need to point out that grain sizes have to be greater than zero after reconstruction from reduced order realizations. To guarantee this, we perform model reduction on the logarithm of grain volume fractions, $\ln(f_{gr,i})$ rather than on $(f_{gr,i})$. To generate a new grain size feature, we draw a sample $\boldsymbol{\xi}$ in the surrogate space, and find its original representation $\mathbf{y}$ in the physical space, which is an array of logarithms of grain volume fractions $\mathbf{y} = \ln(\mathbf{f}_{gr})$. The real grain volume of the microstructure is then $\mathbf{V}_{gr} = V\exp(\mathbf{y})$, where V is the total volume of the microstructure.

6.1. Monte Carlo validation

Monte Carlo simulation is conducted to validate various models on computing the variability of FIPs. The purpose of MC is to validate the performance of the PCA/KPCA model reduction and reconstruction, as well as of the PC expansion. We will see from this section that sampling from the reduced-order space is approximately equivalent to sampling in the physical input space, while the obtained efficiency is significant. We will first project the given microstructure snapshots (input data) to a reduced-order space

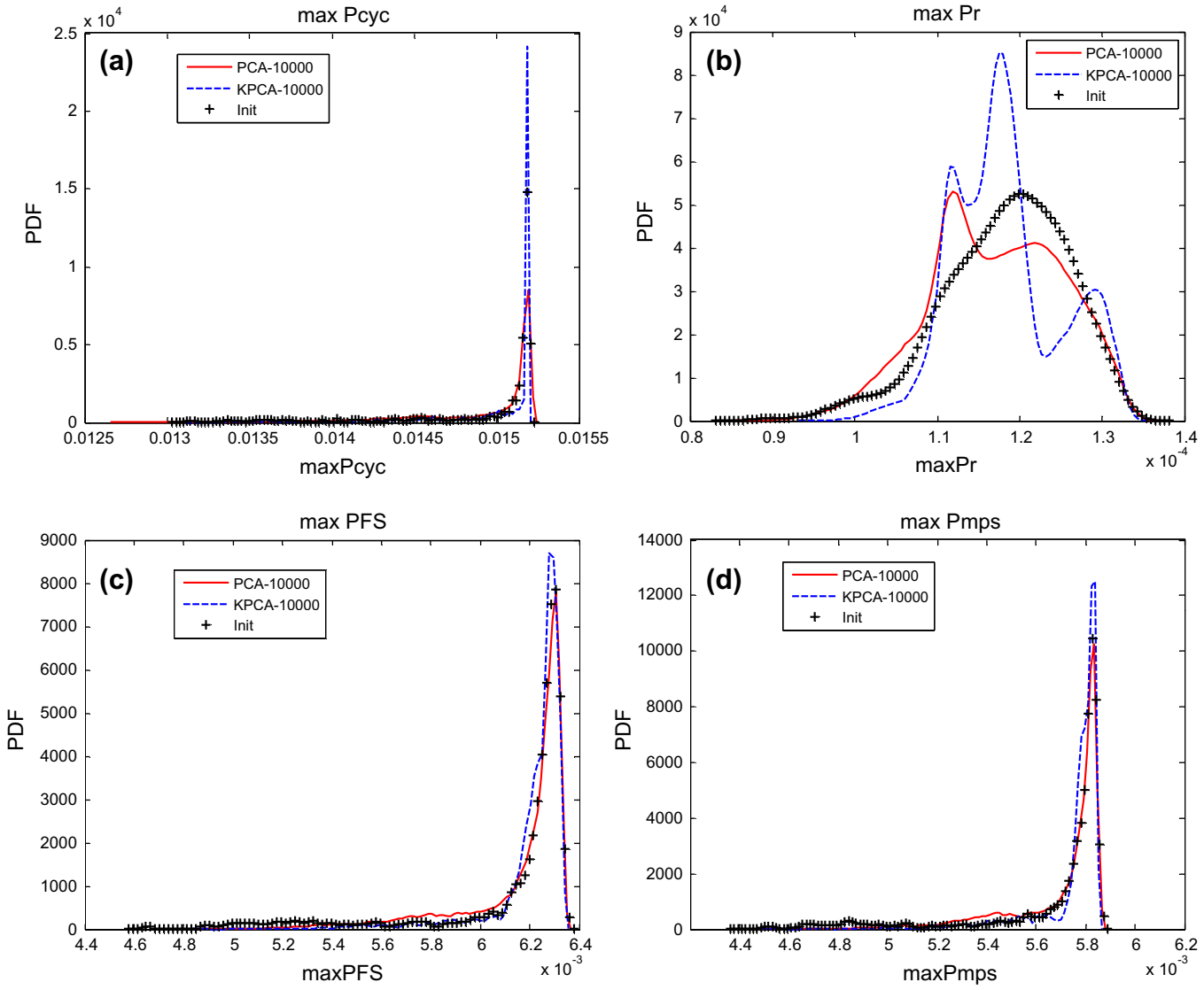

Fig. 13. Distributions of the maximum FIPs computed by different methods. The PDFs marked as 'Init' are computed using the initial given data. For MC, 10,000 samples are drawn in the reduced space and mapped back to the texture input space. A fixed grain volume $V_{gr} = 1.85 \times 10^{-5}$ mm^3 is assigned to all grains. FIPs are computed using the deterministic solver on these reconstructed microstructures and kernel density function is constructed based on data. The dimensionality of the low-dimensional space is 4. (a) *Max* P_{cyc}; (b) *Max* P_r; (c) *Max* P_{FS}; (d) *Max* P_{mps}.

through PCA/KPCA and then map this reduced-order space through PCE to a set of standard Gaussian ($\mathcal{N}(0,I)$) or independent uniform ($\mathcal{U}(-1,1)$) random variables. To generate new microstructure samples, we thus sample Gaussian or uniform distributions. These samples are mapped back to the reduced space derived by PCA/KPCA. Microstructures in the physical input space are then recovered via pre-imaging. The FIPs are evaluated for many randomly generated microstructures and the distributions of these properties will then be constructed through kernel density method and compared with the distributions constructed based on the 1000 initially given samples. The MC results will also be used to verify the ASGC simulations performed later on in this section.

First, we would like to examine which microstructure feature is more substantially affecting the variability of FIPs. To this end, we compute the statistics of FIPs of the 1000 initial samples in three ways.

- Case A: a constant grain size vector is assigned to all the 1000 samples, and the texture varies from sample to sample. Without loosing generality, we assume all grains have the same size (d_{gr} = 0.0265 mm, cube root), while the texture is randomly generated as described above.
- Case B: the grain sizes of different microstructure samples are randomly generated with mean size being 0.0265 mm as mentioned before. A deterministic texture is randomly selected from the 1000 initial samples and assigned to all the microstructures. Therefore, the grain size is the sole source of uncertainty.
- Case C: the 1000 texture samples are one to one linked to the 1000 grain size vectors to define microstructure samples, so that the uncertainty of the two features can be considered simultaneously.

For each of the above cases, we call the deterministic solver 1000 times and extract the values of the FIPs. The volume fraction of primary γ' is 0 and that of secondary and tertiary γ' is set to be 0.42 and 0.11, respectively. The range of the cyclic strain is from -0.007 to 0.007. The strain rate is selected to be 0.001 s^{-1}. By comparing the distributions of the FIPs of these three cases, we find that most of the distributions from Case A are very close to the corresponding distributions from Case C. Also, the variance of FIPs caused by grain size uncertainty (Case B) is much smaller than that caused by orientational uncertainty (Case A). Fig. 7 shows the PDFs of maximum FIPs over microstructure domain constructed based on 1000 initial samples for Case A and Case C, respectively. It is seen that most of the PDFs for the two cases are very close except that $maxP_{cyc}$ shows certain difference.

Comparing the statistics of the three cases (Table 1), we can see that the mean and standard deviation (std) of Cases A and C are very close to each other, while the variance of Case B is much smaller than the other two cases. Therefore, we ignore the grain size uncertainty while putting our focus on the texture uncertainty. This treatment further reduces the dimensionality of the input space without significantly influencing the evaluation of the distribution of the FIPs. As we will see shortly, the reduced

Table 2
Statistics of the maximum FIPs computed by different model reduction techniques with different dimensions. Uniform-Legendre PCs are adopted to map the reduced surrogate space of texture to a uniform distribution $\mathcal{U}(0,I)$. In the table, "Init" refers to the initial 1000 samples, "PCA-4dim" refers to 10,000 MC samples generated in the 4-dimensional reduced space constructed by linear PCA, and "KPCA-4dim" refers to 10,000 MC samples generated in the 4-dimensional reduced space constructed by KPCA. Similar notation is used for the rest of the acronyms.

	Init	PCA-4dim	PCA-5dim	PCA-6dim	KPCA-4dim	KPCA-5dim	KPCA-6dim
Max P_{cyc} mean	1.49×10^{-2}	1.49×10^{-2}	1.49×10^{-2}	1.49×10^{-2}	1.51×10^{-2}	1.51×10^{-2}	1.50×10^{-2}
Max P_{cyc} std	5.02×10^{-4}	4.38×10^{-4}	4.23×10^{-4}	4.35×10^{-4}	2.74×10^{-4}	2.71×10^{-4}	3.29×10^{-4}
Max P_r mean	1.18×10^{-4}	1.17×10^{-4}	1.17×10^{-4}	1.17×10^{-4}	1.18×10^{-4}	1.19×10^{-4}	1.19×10^{-4}
Max P_r std	7.53×10^{-6}	7.97×10^{-6}	7.97×10^{-6}	8.24×10^{-6}	6.49×10^{-6}	6.68×10^{-6}	6.73×10^{-6}
Max P_{FS} mean	6.13×10^{-3}	6.16×10^{-3}	6.16×10^{-3}	6.16×10^{-3}	6.22×10^{-3}	6.22×10^{-3}	6.21×10^{-3}
Max P_{FS} std	3.41×10^{-4}	2.34×10^{-4}	2.27×10^{-4}	2.26×10^{-4}	1.55×10^{-4}	1.54×10^{-4}	1.77×10^{-4}
Max P_{mps} mean	5.67×10^{-3}	5.69×10^{-3}	5.70×10^{-3}	5.70×10^{-3}	5.76×10^{-3}	5.76×10^{-3}	5.75×10^{-3}
Max P_{mps} std	3.03×10^{-4}	2.12×10^{-4}	2.03×10^{-4}	2.08×10^{-4}	1.33×10^{-4}	1.32×10^{-4}	1.59×10^{-4}

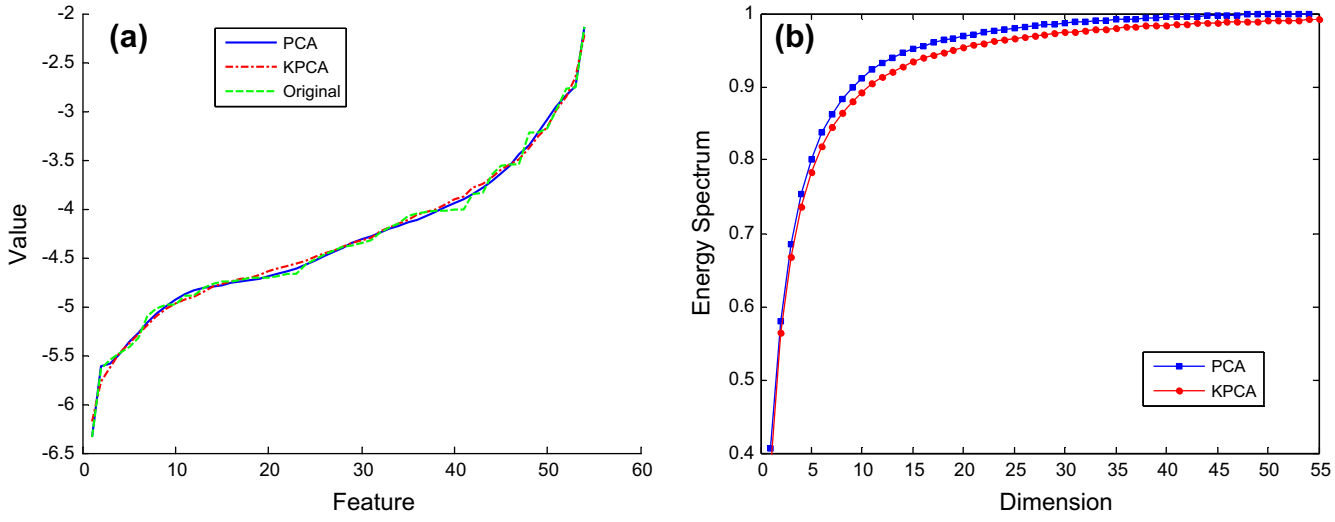

Fig. 14. (a) PCA and KPCA reconstructed grain size feature compared with an original test sample. The dimensionality of the reduced-order representation for both cases is 10, which captures 91.2% and 89.2% of the total "energy", respectively. (b) Plots of the energy spectrum for PCA and KPCA. The value of the *y*-axis is the total energy proportion captured by the first *x* principal components.

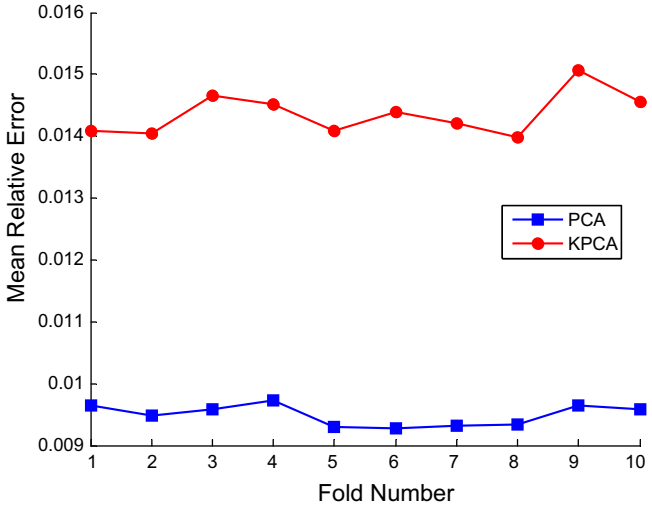

Fig. 15. Averaged relative errors of testing grain size samples in 10-fold cross validation for PCA and KPCA.

dimensionality of the grain size feature is larger than that of texture. However, the variation induced in FIPs is insignificant.

We next examine the model reduction of the input texture space. The randomness will only be assigned to grain orientations, while the volume of all grains is fixed at $V_{gr,i} = 1.85 \times 10^{-5}\,\mathrm{mm}^3$, $i = 1, \ldots, 54$. The total dimensionality of the input microstructure feature is $54 \times 4 = 216$, in which 54 dimensions are fixed grain sizes and the rest 162 dimensions are random orientations. We first construct the reduced model for the 1000 initial microstructure samples. Then, we arbitrarily choose the reduced coordinates for one of the 1000 samples. After that, we reconstruct the microstructure feature (texture) using the chosen reduced coordinates. The reconstructed and the original features are plotted and compared in Fig. 8. We first apply the PCA method to reduce the input space to 4 dimensions driven by the given samples. The total energy proportion, defined by Eq. (57) captured by the largest 4 eigenvalues is 0.918 > 90% (see Fig. 9).

$$\mathrm{Energy}(r) = \frac{\sum_{i=1}^{r} \lambda_i}{\sum_{j=1}^{N} \lambda_j}, \tag{57}$$

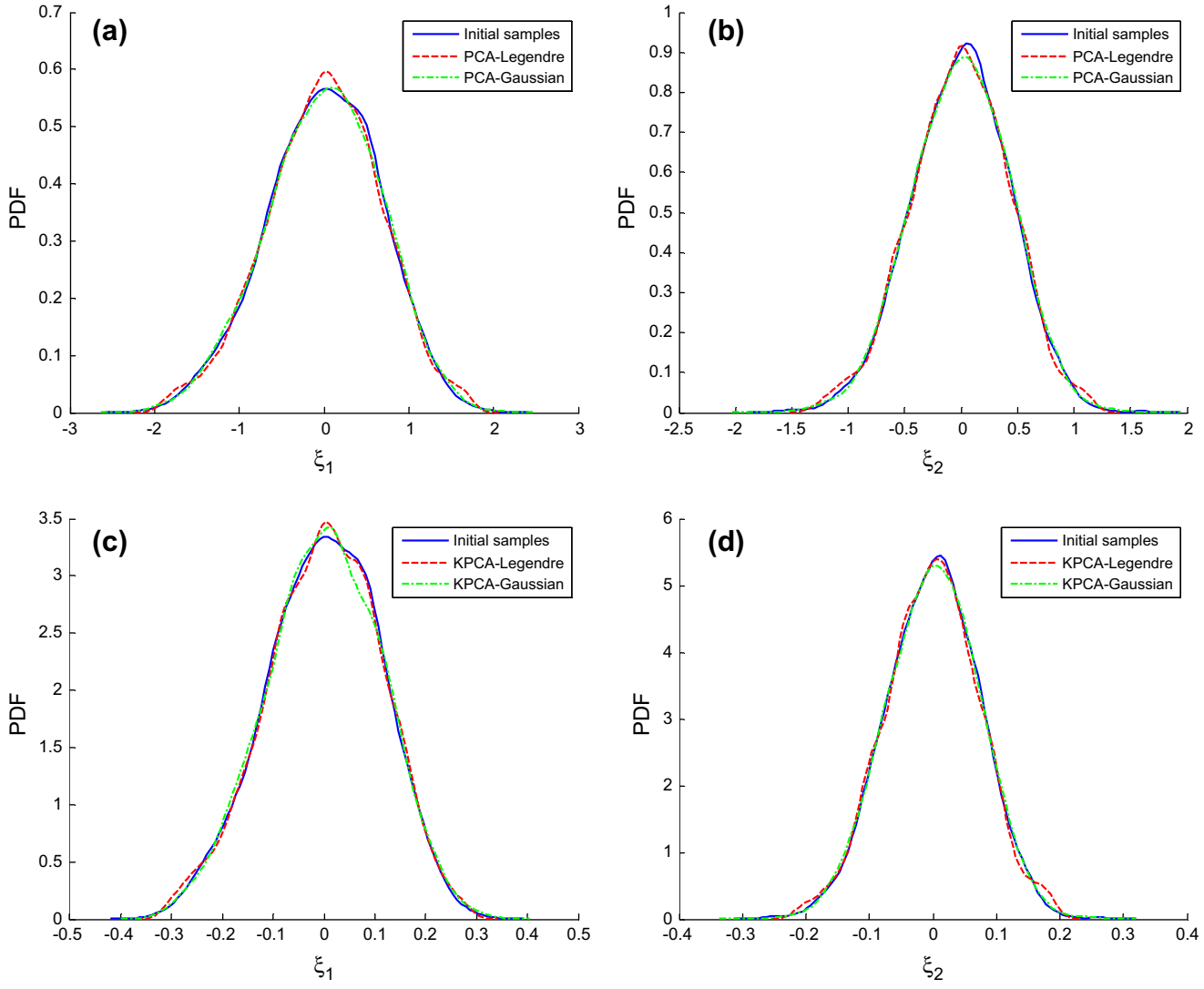

Fig. 16. (a,b) Marginal PDFs of the first 2 PCA reduced initial random variables (the reduced representations obtained after performing PCA on the 1000 given grain size samples) and identified random variables using PCE (reconstructed through PCE (Eq. (26)) on 10,000 randomly generated samples from Gaussian or Uniform distribution). (c,d) Marginal PDFs of the first 2 KPCA reduced random variables and identified random variables using PCE on 10,000 randomly generated samples from Gaussian or Uniform distribution. The distributions are constructed through kernel density based on data.

where r is the number of preserved largest eigenvalues λ_i and N is the number of given samples. A reconstructed realization compared with the original texture is depicted in Fig. 8a. We next repeat the above calculations using KPCA to perform the non-linear model reduction of the input texture samples. The parameter c in the kernel width σ estimation Eq. (25) is chosen to be 10. The total energy captured by the largest 4 eigenvalues is 0.815, which is lower than that captured in linear PCA. A reconstructed realization compared with the original microstructure feature is depicted in Fig. 8b. Both of the two model reduction techniques demonstrate good capability of reducing and reconstructing microstructure features.

The energy spectrum of both linear PCA and kernel PCA are plotted. It is observed that the first few eigenvalues capture the majority of the total energy and PCA eigenvalues capture more energy than KPCA at the same dimension.

We next conduct a 10-fold cross validation on the 1000 initial samples to test the performance of the two model reduction schemes on the texture microstructure feature. For the first fold, 100 out of 1000 samples are used as the testing set to test the reconstructed features from the PCA/KPCA model trained by the remaining 900 samples. Then, we select another (different) 100 samples as the testing set, and the rest 900 to be the training set. The process is repeated 10 times until we have used all the 1000 samples as testing sample once. The average of the relative errors between testing and reconstructed features is defined as

$$Err_{\text{test}} = \frac{1}{N'}\sum_{i=1}^{N'}\epsilon_i,$$
$$\epsilon_i = \frac{\|\mathbf{y}_i - \hat{\mathbf{y}}_i\|_{L_2}}{\|\mathbf{y}_i\|_{L_2}}, \tag{58}$$

where $\mathbf{y}_i$ and $\hat{\mathbf{y}}_i$ are the testing samples and predicted features, respectively, and N' is the size of the testing set. The averaged relative errors for texture are plotted in Fig. 10. The mean error is 0.1201 for PCA and 0.1462 for KPCA. It is observed that the error of PCA is smaller than that of KPCA, while both of them are below 15% when four principal components are preserved.

We next need to establish the mapping between the low-dimensional surrogate space and a well-defined probabilistic distribution. By the independence assumption between the random variables in the reduced-order representation, each component

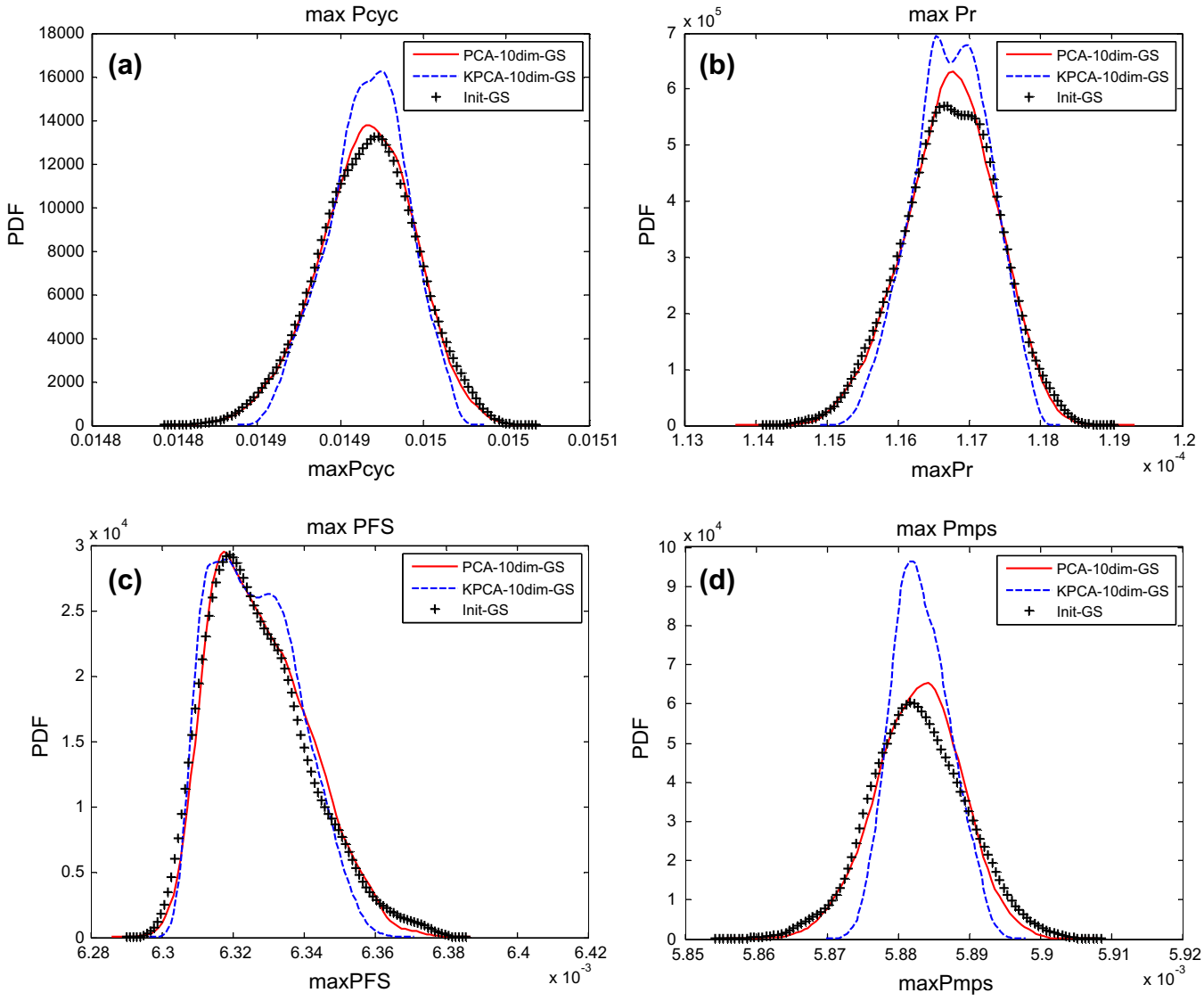

Fig. 17. Distributions of the maximum FIPs due to grain size uncertainty computed by different methods. For MC, 10,000 samples are drawn in the 10-dimensional reduced space and mapped back to the grain size input space. (a) *Max* P_{cyc}; (b) *Max* P_r; (c) *Max* P_{FS}; (d) *Max* P_{mps}.

can be approximated using one-dimensional PC basis of degree p. If Gaussian random variables are to be mapped then Hermite polynomials are chosen to be the PC basis. On the other hand, if the reduced space is mapped to a uniform distribution, Legendre polynomials must be selected for Eq. (26). We here use the Gaussian–Hermite and Uniform-Legendre PCs, respectively, for different model reduction schemes and compare the reconstructed features. The order of PC basis is set to be 12, which gives accurate estimation to the reduced-order representation distributions (Figs. 11 and 12). The distributions of the initial reduced variables of microstructure features are computed from the given 1000 initial samples based on the histogram of the reduced samples derived by PCA/KPCA (Eq. (15)). Alternatively, 10,000 random variables are randomly sampled from the uniform or Gaussian distribution and mapped to the surrogate space via PCE (Eq. (26)). It is noticed that Uniform-Legendre PCs give accurate representation to all four reduced-order random variables, while Gaussian–Hermite cannot fit the random variable ξ_2 corresponding to the second principal component very well. Thus, we will next perform further stochastic simulations using only Uniform-Legendre PCs.

The marginal PDFs of the maximum FIPs of microstructures satisfying given texture constraints computed by Monte Carlo using 10,000 samples from the reduced space are plotted in Fig. 13, as well as the distributions of the FIPs computed directly from the 1000 initial samples with various texture and fixed grain size (the same distribution obtained in Case A). Uniform-Legendre PCs are used to represent the reduced random variables. The agreement of MC simulated PDFs using 10,000 samples and the PDFs obtained using the given initial 1000 samples is achieved, which validates the performance of model reduction. Both PCA and KPCA capture the main features of the PDFs of the FIPs. The PCA results seem to be more consistent with the initial samples.

The sampled mean and standard deviation of the maximum FIPs obtained from different methods (some to be discussed later on) are listed in Table 2. Most of the MC simulated statistics, especially the means, agree quite well with the ones computed directly from the 1000 initial data considering that only 4 random variables are used to generate new samples. The PCA simulation gives closer prediction to the sampled mean and variance obtained using only the initial samples.

Following the same idea as for the texture, model reduction of the grain size feature is also studied. Again, we assume only secondary and tertiary γ' precipitates dispersed in the γ matrix with fixed volume fractions (setting $f_{p1} = 0$, $f_{p2} = 0.42$ and $f_{p3} = 0.11$), so

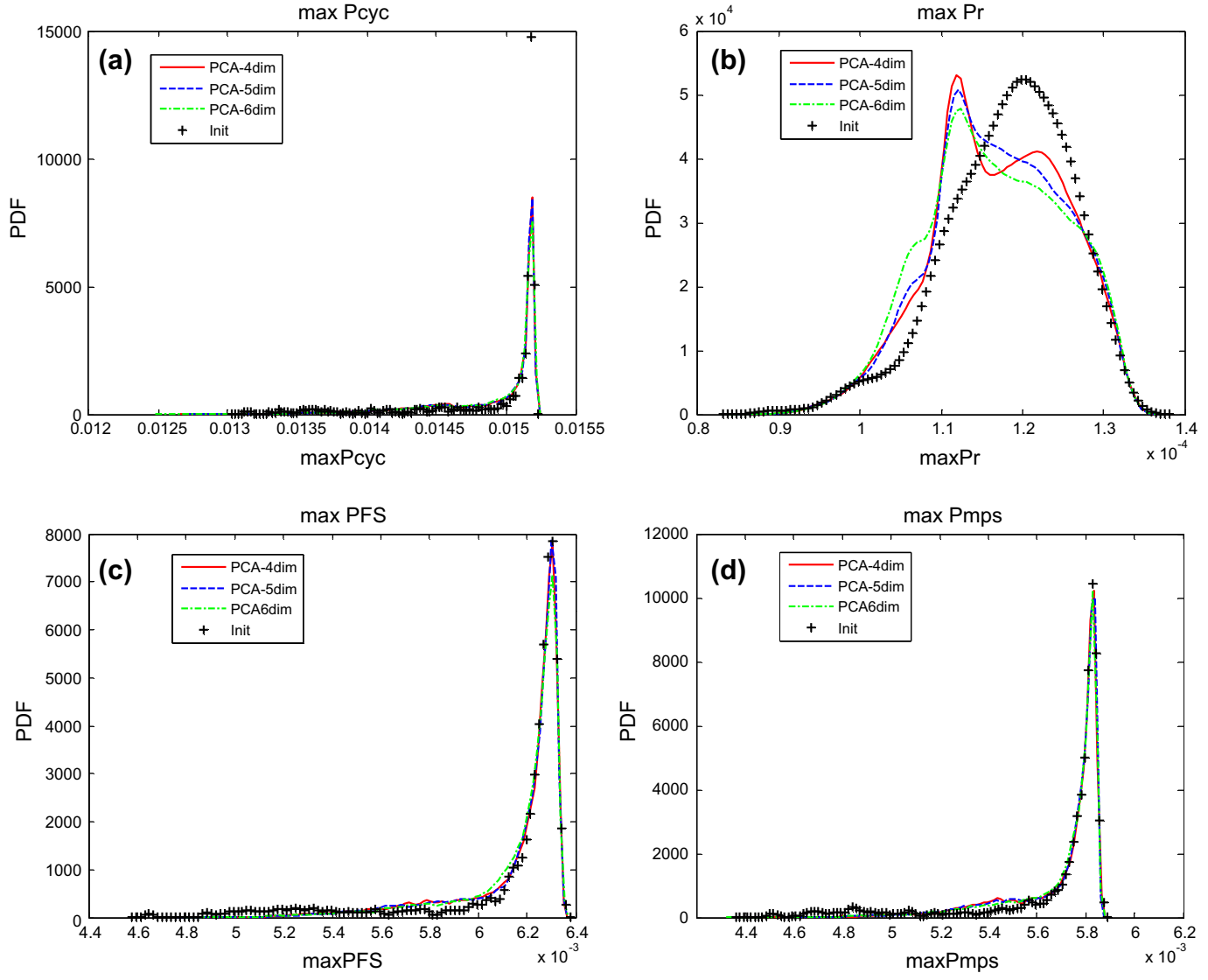

Fig. 18. Distributions of maximum FIPs of 10,000 MC samples computed based on PCA and Uniform-Legendre PCE. The dimensionality of the reduced space varies from 4 to 6. The distributions of FIPs of 1000 initial samples are also plotted as a reference. (a) *Max* P_{cyc}; (b) *Max* P_r; (c) *Max* P_{FS}; (d) *Max* P_{mps}.

that the grain size effect can be captured. An arbitrary but deterministic texture is assigned to all 1000 initial samples, whose grain sizes are generated using the procedure described earlier with mean size 0.0265 mm. The dimensionality of the random input is now 54. To guarantee that the grain sizes are positive, we first transform all grain volume fractions to logarithms. PCA/KPCA is then used to compute the low-dimensional surrogate space of the transformed grain sizes. New grain size samples are generated by sampling in the reduced space and mapped back to the physical space. The grain volume vector $\mathbf{V}_{gr}$ corresponding to a low-dimensional representation ξ is computed as

$$\mathbf{V}_{gr} = V\exp(\Gamma^{-1}(\xi)), \tag{59}$$

where Γ is the PCA/KPCA model reduction map of the logarithmic volume fraction to the low-dimensional space as defined in Eq. (15), and $V = 0.001$ mm^3 is the total volume of the microstructure. We first apply the PCA method to reduce the dimensionality of the stochastic input space. The correlation between grain size samples is weak since they are generated in a very random way. This correlation is still captured by PCA even though the grain size generation procedure is not known during model reduction. We must keep the first 10 principal components to capture more than 90% of the "energy". The total energy proportion captured by the largest 10 eigenvalues is 0.912. Using KPCA, the non-linear model reduction captures 0.892 of the total energy by the largest 10 eigenvalues. The energy captured by the same number of eigenvalues in PCA is close to that in KPCA for the grain size feature. Reconstructed realizations by PCA and KPCA compared with the original grain size feature are depicted in Fig. 14a. The newly sampled grain size features are smoother than the initial samples. Both model reduction techniques demonstrate good capability of reducing and reconstructing the grain size feature. The energy spectrums of both PCA and KPCA are shown in Fig. 14b. It is observed that the first few eigenvalues capture the majority of the total energy and PCA eigenvalues capture a little more energy than KPCA at the same dimensionality.

The 10-fold cross validation for grain size feature is shown in Fig. 15. The relative error for both cases is smaller than 1.6% with PCA performing better than KPCA.

Polynomial chaos representation on reduced random variables is also tested with 10,000 random samples in the reduced space. The order $p = 12$ can accurately capture the distributions of all the reduced random variables derived from the initial samples. In Fig. 16, we show PC expansion of the first 2 random variables who have the largest variance for both PCA and KPCA. The agreement

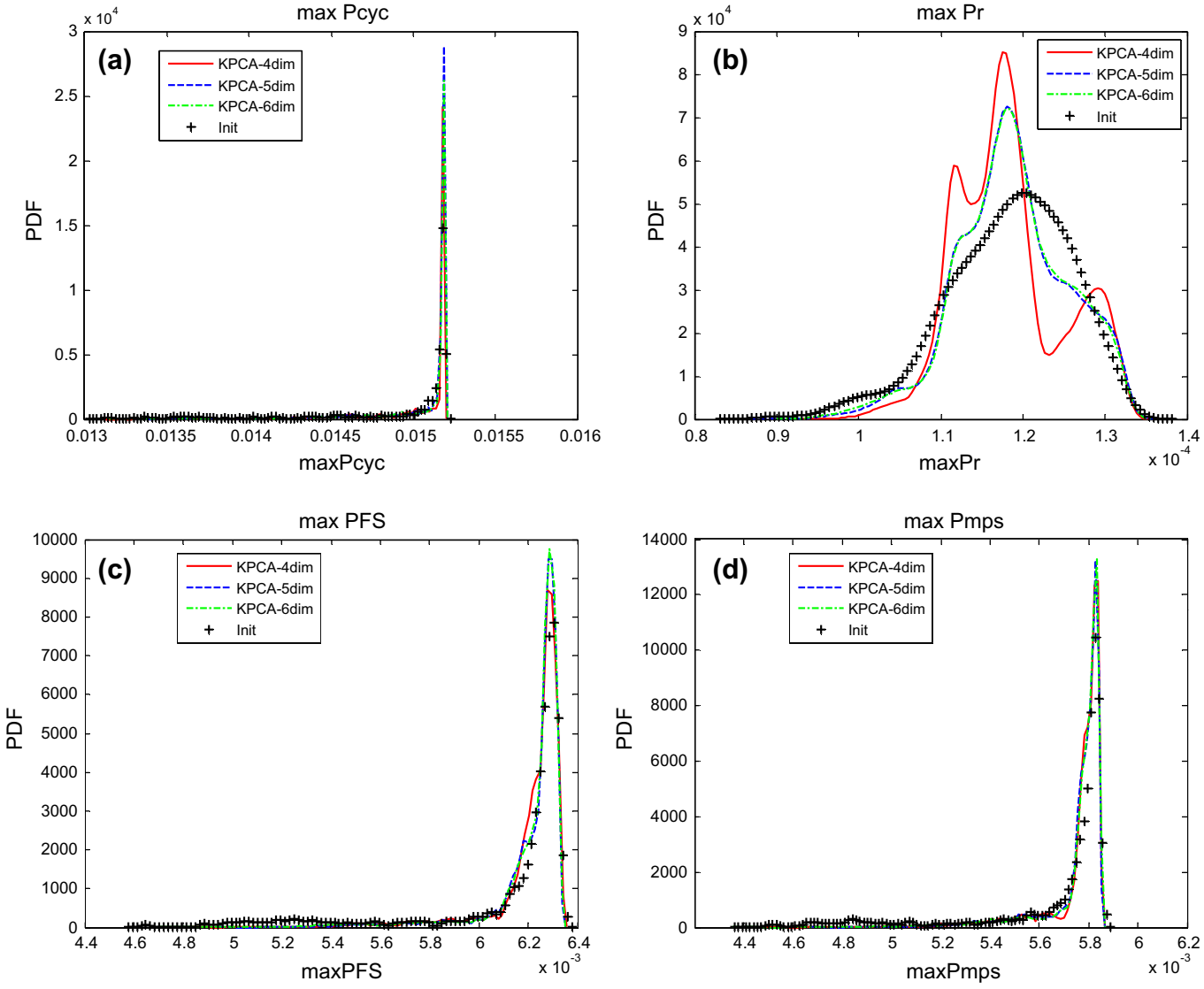

Fig. 19. Distributions of maximum FIPs of 10,000 MC samples computed based on KPCA and Uniform-Legendre PCE. The dimensionality of the reduced space varies from 4 to 6. The distributions of FIPs of 1000 initial samples are also plotted as a reference. (a) *Max* P_{cyc}; (b) *Max* P_r; (c) *Max* P_{FS}; (d) *Max* P_{mps}.

between identified and initial random variables distributions is observed. Both Unform-Legendre and Gaussian–Hermite PCs give accurate estimation on the distributions. To be consistent with the texture computation, we adopt Uniform-Legendre PCE to map the reduced space to a uniform distribution where new samples will be generated.

The reconstructed distributions of the FIPs and those directly extracted from the initial samples (Case B: fixed texture, random grain sizes) are plotted in Fig. 17. We notice that the variance of FIPs induced by the grain size effect is very small just as we discussed earlier (one order of magnitude smaller than texture induced standard deviation as shown in Table 1). The PCA gives very accurate prediction to the initial data, while KPCA captures well the main characters but provides slightly different estimation to the variance.

We also discover that the reduced dimensionality of the grain size feature is 10, which is much larger than the texture feature 4 dimensions were enough for texture reduction in capturing 90% energy. It is inefficient to explore high-dimensional stochastic input space to capture very small variability in the properties. Therefore, we will focus on texture uncertainty in the following examples.

Convergence tests as the dimension of the reduced order space increases are performed for PCA and KPCA on the texture feature. The Uniform-Legendre PCs are used. We plot the marginal PDFs of maximum and volume averaged FIPs extracted from 10,000 MC samples when 4, 5 and 6 principal components are preserved in Figs. 18 and 19, respectively, for PCA and KPCA. Placed in the figures are also the distributions of FIPs obtained using only the initial samples (Case A: random texture and fixed grain sizes). We observe great consistence of the simulations with increasing dimensionality of both PCA and KPCA.

The sampled mean and standard deviation of the maximum FIPs computed using different methods and different reduced dimensions are listed in Table 2. It is observed that all the examples (from $r = 4$ to $r = 6$) give consistent prediction, while the PCA predictions are closer to the FIPs obtained using only the initial samples. Improvement on the predicted FIPs is observed as the dimensionality of the reduced space increases, especially for $maxP_r$.

The convergence test of MC simulations as we increase the number of samples is conducted at $r = 6$ (Figs. 20 and 21). Good convergence is achieved using 10,000 random samples.

It was shown that both PCA and KPCA provide good prediction on FIPs distributions and low-order statistics. In most cases, PCA

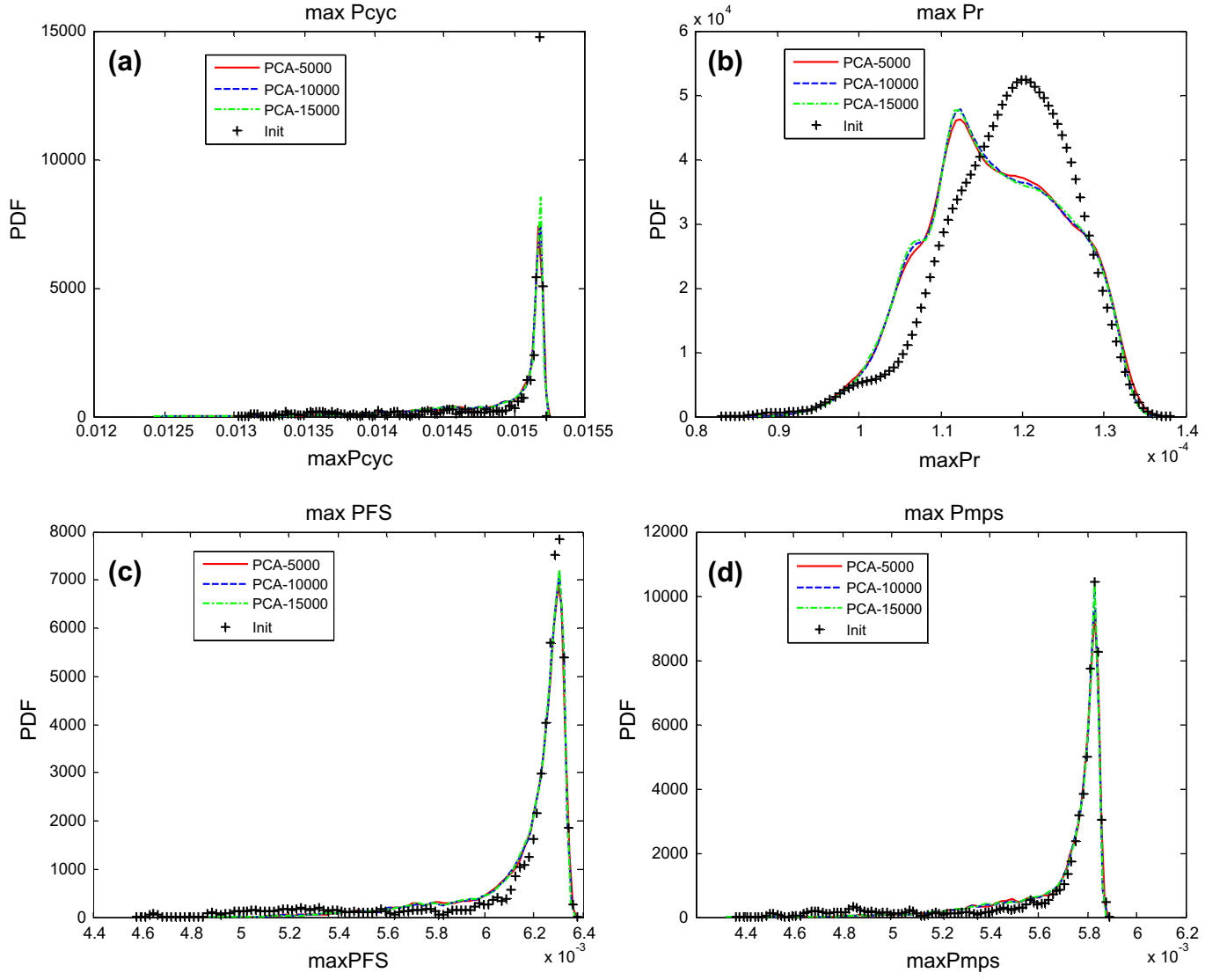

Fig. 20. Convergence test of the distributions of maximum FIPs computed by PCA. 5000, 10,000, and 15,000 samples are generated in the 6-dimensional reduced space. Comparison with 1000 initial samples is shown. (a) *Max* P_{cyc}; (b) *Max* P_r; (c) *Max* P_{FS}; (d) *Max* P_{mps}.

gives closer prediction on mean and standard deviation of FIPs than KPCA at the same reduced dimensionality for the current microstructure data set. This is a bit surprising result considering that KPCA is a non-linear dimensionality reduction method. The reasons for this outcome may include: (1) the variation of the initial samples is too small to show the non-linear nature of the microstructure data; (2) the accuracy of the K nearest neighborhood pre-imaging strategy adopted is not good enough to provide precise microstructure reconstruction; (3) the kernel selected here could not effectively reduce the non-linearity of the data. Moreover, the MC prediction of the mean FIPs is consistent with the initial samples, while the standard deviation prediction contains small deviation.

6.2. Adaptive sparse grid collocation

The variability of FIPs is also examined through the adaptive sparse grid collocation (ASGC) method, which has been proved to be more efficient then Monte Carlo method for stochastic problems of moderately high dimensionality and at the same time provides control of the interpolation error in the stochastic support space [7]. Essentially sparse grids construct an interpolant of the function of interest in the multi-dimensional stochastic space. As before, Uniform-Legendre PCs are adopted to expand the reduced-order texture features as they produce better reconstruction of the reduced random variable distributions. Both PCA and KPCA are employed. The uncertainty source is assumed to be texture whose reduced dimensionality varies from 4 to 6. In sparse grid collocation, the functions of interest (here the FIPs) $u(t,\xi)$ are approximated by

$$\hat{u}_{d,q}(t,\xi) = \sum_{\|\mathbf{i}\| \leqslant d+q} \sum_{\mathbf{j}\in B_i} \omega_{\mathbf{j}}^{\mathbf{i}}(t)\cdot a_{\mathbf{j}}^{\mathbf{i}}(\xi). \tag{60}$$

The mean of the random solution is evaluated as:

$$E(\hat{u}_{d,q}(t)) = \sum_{\|\mathbf{i}\| \leqslant d+q} \sum_{\mathbf{j}\in B_i} \omega_{\mathbf{j}}^{\mathbf{i}}(t)\cdot \int_{\mathscr{L}} a_{\mathbf{j}}^{\mathbf{i}}(\xi)d\xi, \tag{61}$$

where q is the depth (level) of sparse grid interpolation and d is the dimensionality of the stochastic space. B_i is a multi-index set. $\omega_{\mathbf{j}}^{\mathbf{i}}$ is the hierarchical surplus, which is the difference between the function value $u(t,\xi)$ at the current point ξ and interpolation value $\hat{u}_{d,q-1}(t,\xi)$ from the coarser grid in the previous level. $a_{\mathbf{j}}^{\mathbf{i}}$ is the

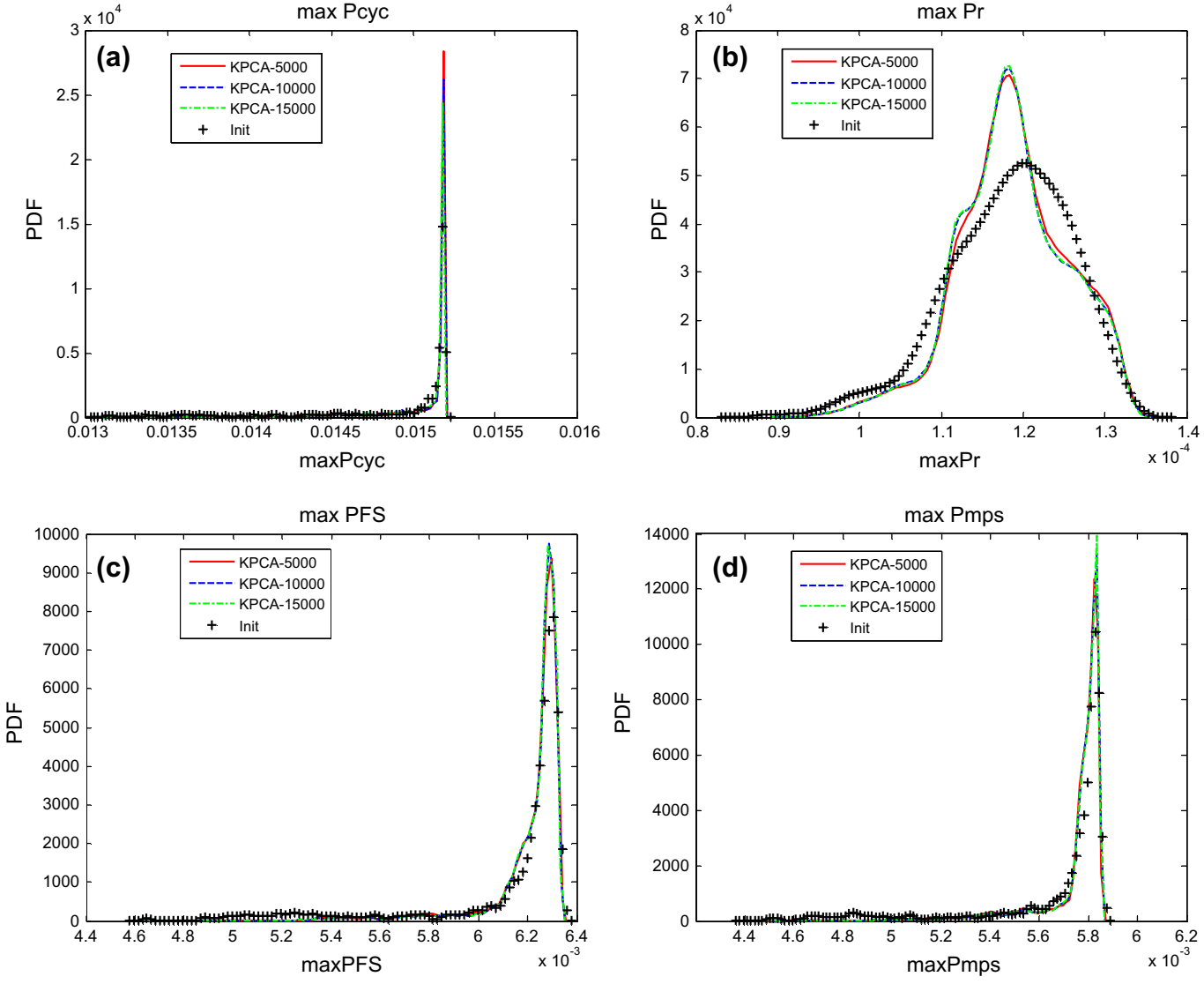

Fig. 21. Convergence test of the distributions of the maximum FIPs computed by KPCA. 5000, 10,000, and 15,000 samples are generated in the 6-dimensional reduced space. Comparison with 1000 initial samples is shown. (a) *Max* P_{cyc}; (b) *Max* P_r; (c) *Max* P_{FS}; (d) *Max* P_{mps}.

d-dimensional multilinear basis functions defined by tensor product. For the estimation of higher-order moments (kth order) of the function of interest, we only need to change u to u^k. The function of interest u and its interpolation $\hat{u}$ in the current work are the maximum and volume averaged FIPs of the microstructure. The threshold of the error indicator, defined in Eq. (62), for adaptivity is set to be 10^{-4} for all computations. The error indicator $\gamma_{\mathbf{j}}^{\mathbf{i}}$ measures the contribution of each term in Eq. (61) to the integration value (mean of the interpolated function) relative to the overall integration value computed from the previous interpolation level. For error higher than the threshold at a given point in the sparse grid, new support nodes will be added in the neighborhood of this point at the next level of interpolation [7]:

$$\gamma_{\mathbf{j}}^{\mathbf{i}} = \frac{\|\omega_{\mathbf{j}}^{\mathbf{i}} \cdot \int_{\mathscr{L}} a_{\mathbf{j}}^{\mathbf{i}}(\xi) d\xi\|_{L_2}}{\|E_{\|\mathbf{i}\|-d-1}\|_{L_2}}. \tag{62}$$

We first focus only on texture uncertainty induced variability of the FIPs. When PCA is adopted, the ASGC error converges below 10^{-4} at level 8, namely, no new collocation nodes will be needed after level 8. Total number of 1399, 3059, and 6220 collocation nodes are generated, respectively, for reduced space of dimensionality 4, 5, and 6. Note that each collocation point requires the solution of the material point simulator for given realizations of the random variables.

The marginal PDFs of maximum FIPs when different number of principal components are preserved are plotted in Fig. 22. The construction of the distributions of the FIPs is a post processing operation in the ASGC method. After performing the ASGC simulation, we uniformly sample 10,000 random points in the hypercube where the sparse grid is defined. The FIPs corresponding to each point are computed by interpolation using the basis obtained from ASGC. Kernel density functions based on histograms of the samples of the FIPs are therefore constructed. Comparison with MC simulation when the reduced-order space is 6-dimensional is demonstrated. We would like to point out that the data of MC used here are identical with those in the earlier examples. They are re-plotted here just for comparison purposes. ASGC distributions show similar shapes with the results of MC simulations. However, distributions of the FIPs predicted by ASGC are broadened (larger variance) as we increase the dimensionality of the reduced space.

Using KPCA, the marginal PDFs of maximum FIPs with different number of retained principal components are also extracted and

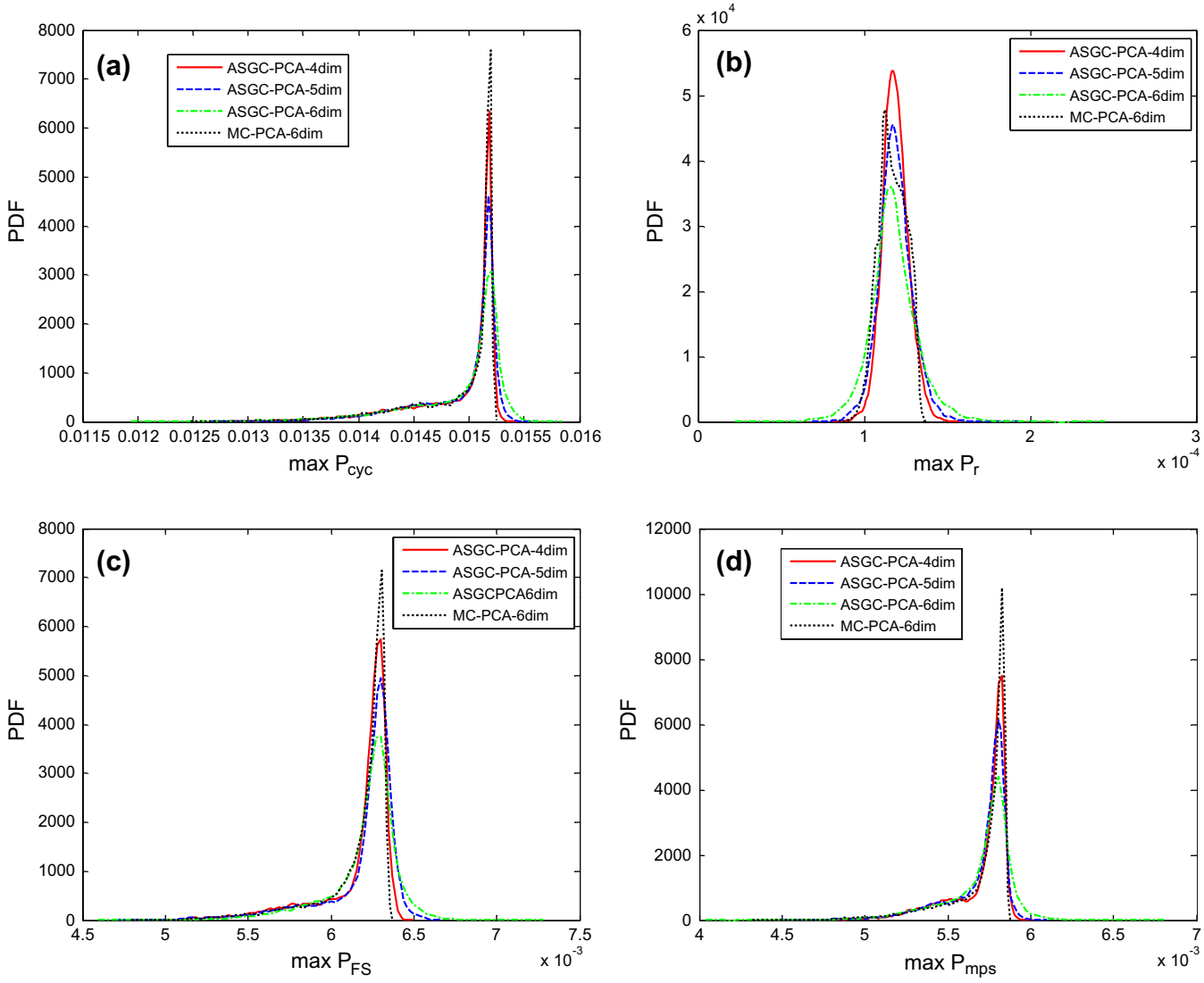

Fig. 22. Distributions of maximum FIPs obtained with ASGC based on linear PCA and Uniform-Legendre PCE. Comparison with 10,000 MC samples at $r = 6$ is demonstrated. (a) *Max* P_{cyc}; (b) *Max* P_r; (c) *Max* P_{FS}; (d) *Max* P_{mps}.

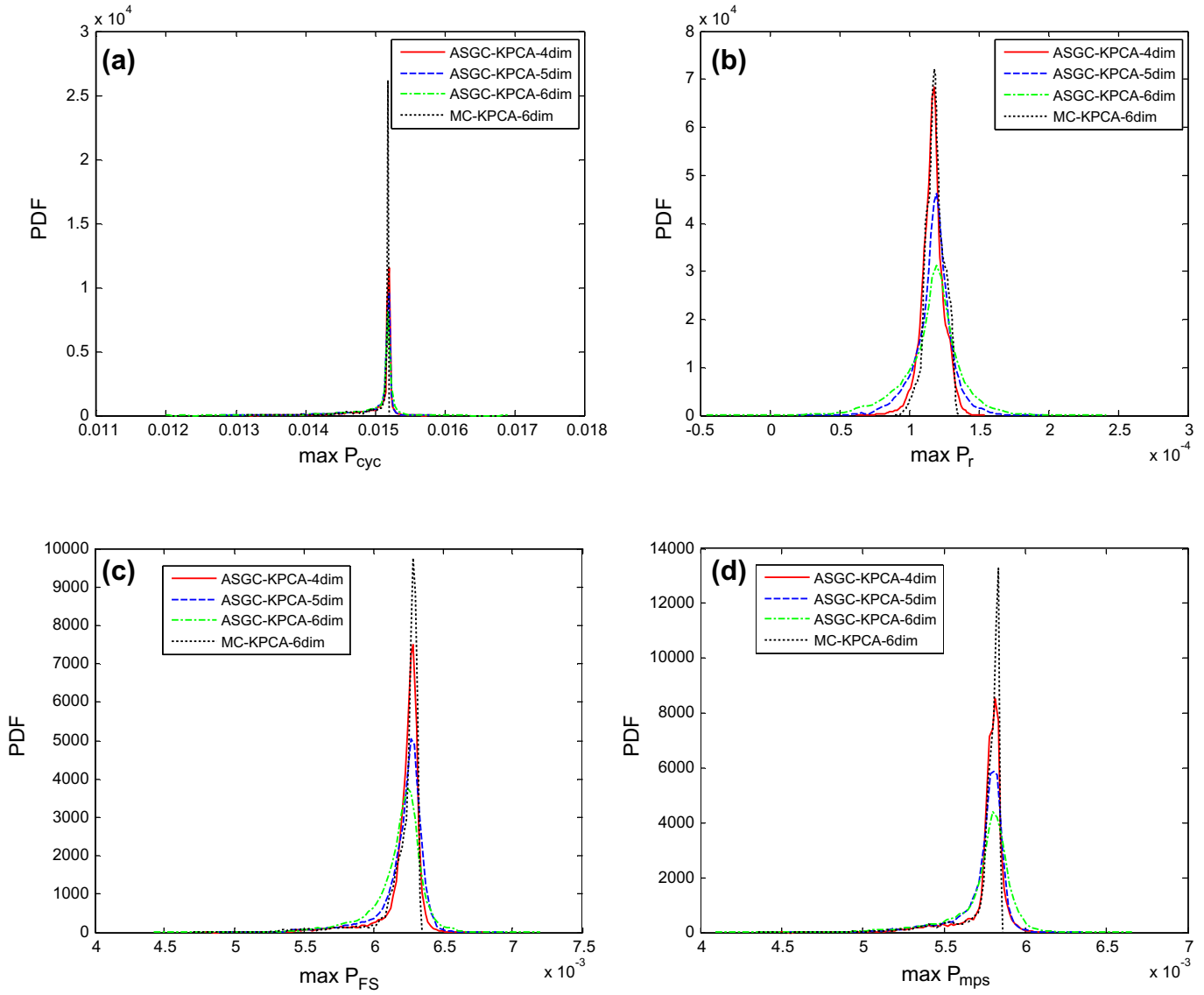

Fig. 23. Distributions of the maximum FIPs obtained with ASGC based on KPCA and Uniform-Legendre PCE. Comparison with 10,000 MC samples at $r = 6$ is demonstrated. (a) *Max* P_{cyc}; (b) *Max* P_r; (c) *Max* P_{FS}; (d) *Max* P_{mps}.

presented in Fig. 23. The number of collocation points for $r = 4$ and $r = 5$ after convergence at level 9 is 1647, 3633, respectively. For $r = 6$, 7921 collocation points are generated up to level 10.

The statistics of the maximum FIPs evaluated by ASGC combined with Uniform-Legendre PCE are tabulated in Table 3. Again, the ASGC simulations provide close estimation of mean values with MC, while the standard deviation demonstrates some small difference.

The distributions of the FIPs (Figs. 22 and 23) become slightly broader as the dimensionality of the reduced space increases. However, the predicted standard deviation (Table 3) does not show this trend. Moreover, most MC predicted PDFs of FIPs are narrower than the ASGC constructed FIPs. However, the MC computed standard deviation of certain FIPs is larger than that evaluated through ASGC. This possible inconsistency may arise from insufficient samples at the tails of the distributions and a need for a higher depth of

Table 3
Mean and standard deviation of the maximum FIPs evaluated by ASGC. Uniform-Legendre PCE is employed.

	PCA-4dim	PCA-5dim	PCA-6dim	KPCA-4dim	KPCA-5dim	KPCA-6dim
Max P_{cyc} mean	1.49×10^{-2}	1.49×10^{-2}	1.49×10^{-2}	1.51×10^{-2}	1.50×10^{-2}	1.50×10^{-2}
Max P_{cyc} std	4.13×10^{-4}	3.92×10^{-4}	4.29×10^{-4}	2.61×10^{-4}	2.48×10^{-4}	3.09×10^{-4}
Max P_r mean	1.18×10^{-4}	1.19×10^{-4}	1.17×10^{-4}	1.17×10^{-4}	1.17×10^{-4}	1.17×10^{-4}
Max P_r std	9.29×10^{-6}	1.09×10^{-5}	1.17×10^{-5}	5.57×10^{-6}	1.01×10^{-5}	1.09×10^{-5}
Max P_{FS} mean	6.17×10^{-3}	6.19×10^{-3}	6.20×10^{-3}	6.22×10^{-3}	6.21×10^{-3}	6.18×10^{-3}
Max P_{FS} std	2.33×10^{-4}	2.31×10^{-4}	2.07×10^{-4}	1.26×10^{-4}	1.31×10^{-4}	9.17×10^{-5}
Max P_{mps} mean	5.70×10^{-3}	5.70×10^{-3}	5.70×10^{-3}	5.76×10^{-3}	5.74×10^{-3}	5.74×10^{-3}
Max P_{mps} std	1.86×10^{-4}	1.69×10^{-4}	1.30×10^{-4}	1.11×10^{-4}	6.75×10^{-5}	9.77×10^{-5}

interpolation in ASGC. For this problem, the ASGC estimation balances computational accuracy and efficiency.

All the above examples assume constant volume fractions of secondary and tertiary γ' precipitates, and the primary precipitates are not considered. Next, we take volume fractions of secondary and tertiary γ' precipitates as sources of uncertainty. The formulation of the current constitutive model adopts volume fractions of different types of γ' precipitates as explicit parameters. Therefore, the randomness of γ' can be easily dealt without the assistance of model reduction. We assume that the volume fractions of the secondary and tertiary γ' particles follow uniform distributions $\mathscr{U}(0.3, 0.5)$ and $\mathscr{U}(0.11, 0.14)$, respectively. The volume fractions are assumed independent from each other as well as from other features (e.g. texture). The reduced space of texture is chosen to be 4. Therefore, the total dimensionality of the sampling space will be 4 + 2 = 6. The PDFs of FIPs computed by both ASGC and MC based on PCA and Uniform-Legendre PCE are plotted in Fig. 24. For a level of interpolation 8, 2939 deterministic problems are solved up in ASGC and 10,000 simulations are conducted in MC. It is seen that the mean and standard deviation of FIPs are different from previous examples because of the varying volume fraction of γ' phase.

6.3. Convex hull of FIPs

To better understand the extreme values of FIPs and learn the correlation between them, convex hulls that serve as envelopes of the values of the FIPs in the presence of uncertainties are constructed. From Eqs. (53) and (54), we see that P_{FS} and P_{mps} are closely correlated, since the latter is a special situation of the former (when $\sigma_n^{max} = 0,\ P_{FS} = P_{mps}$). Therefore, only the 3D visualization of the convex hulls consisting of P_{cyc}, P_r and P_{FS} are shown in Fig. 25. For all the figures, Uniform-Legendre PCs are used to represent the 4-dimensional reduced-order random variables. The points in the FIP coordinate system are the ones that have been used for the construction of the PDFs. The Q-Hull [46] MatLab package is used to construct the convex hull.

It is observed that the volume of the convex hulls predicted by ASGC is greater than the corresponding volume constructed by MC, while the shapes of the convex hulls are similar (Fig. 25). We also recall from the marginal PDFs of FIPs (e.g. Figs. 22 and 23) that the ASGC provides some predictions that are away from the MC predictions but with very low probability (the tails of those PDFs). These less-probable values are the cause of the wide range of the obtained convex hulls. To better demonstrate and understand this

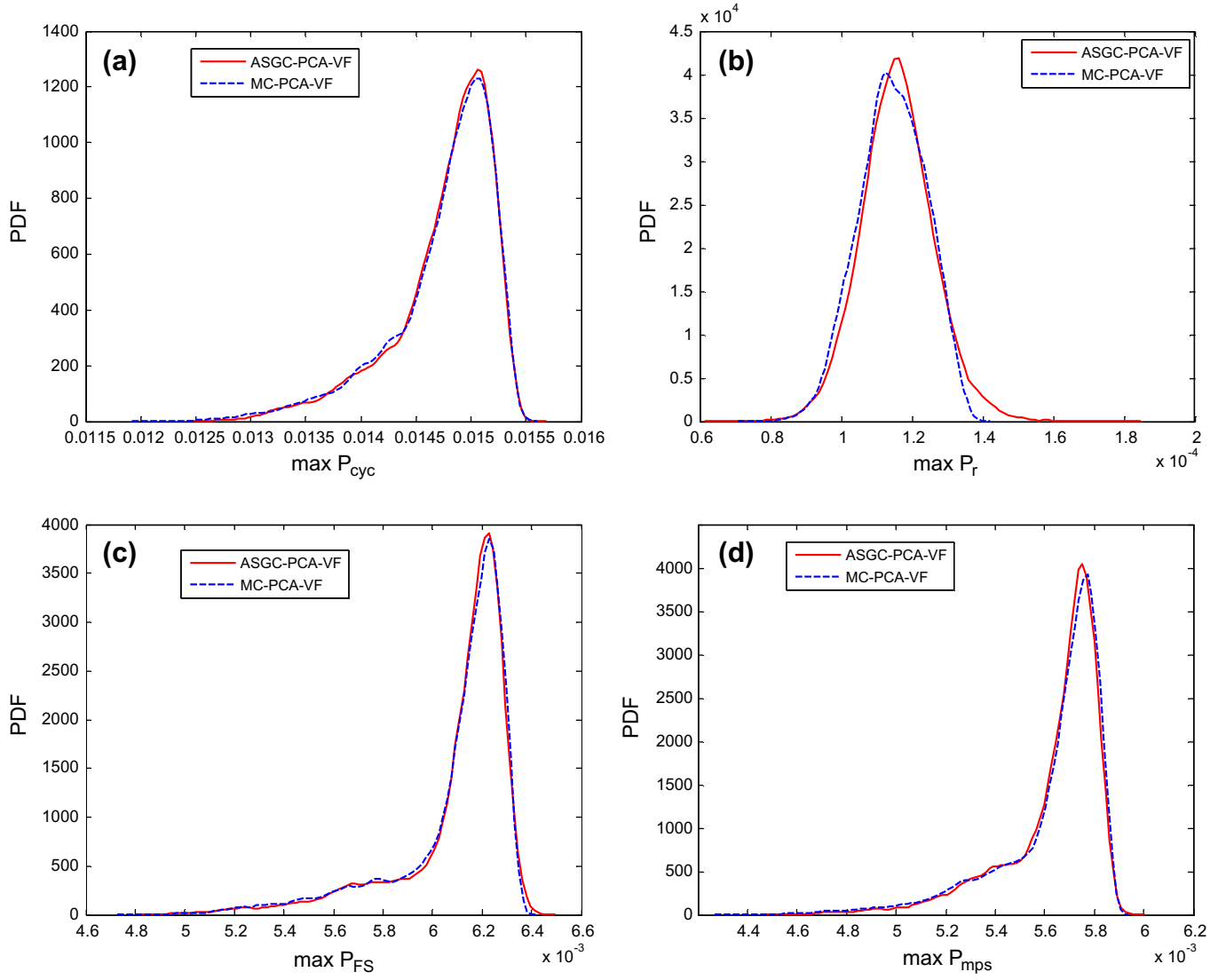

Fig. 24. Distributions of the maximum FIPs obtained by ASGC and 10,000 MC samples when the volume fractions of secondary and tertiary γ' precipitates are random. (a) *Max* P_{cyc}; (b) *Max* P_r; (c) *Max* P_{FS}; (d) *Max* P_{mps}.

phenomenon, we further plot planar convex hulls of two FIPs along with the sample points and PDFs of each dimension (Fig. 26). The correspondence of the low probability and the extreme values predicted by ASGC are clearly captured. (see Fig. 27)

It is seen that most of the data fall within the range where both ASGC and MC give high probability. Finally, 3D and 2D convex hulls when volume fractions of secondary and tertiary γ' precipitates are taken as uncertainty sources are presented. PCA in combination with Uniform-Legendre PCE is employed. The range and shapes of the convex hulls are much different from the cases where γ' volume fractions are taken as constant. (see Fig. 28)

7. Conclusions

In this paper, the effect of multiple sources of uncertainty on two-phase superalloy microstructure fatigue properties is studied. A two-phase microstructure is considered as a combination of random features consisting of grain size, texture, and volume fraction of the γ' phase. Given a set of microstructure samples, PCA based dimensionality reduction techniques are applied to find their underlining correlations. Both linear and non-linear (kernel) PCA methods are examined. The reduced-order representations are mapped to uniform distributions by PC expansion. Adaptive sparse grid collocation is then introduced to sample new microstructures from the low-dimensional space. The strain-based fatigue indicator parameters of superalloy microstructures satisfying given information are computed and their distributions are constructed. The significance of different feature effect on FIPs is examined. It is shown that texture and volume fraction of γ' precipitates are the primary factors determining FIPs in the problems and data considered. The model reduction techniques greatly simplified the representation of random microstructure features, while important characteristics of microstructures are preserved. Convergence with the dimensionality of the reduced-order variables is shown. Comparisons with MC results are also provided. The propagation of uncertainty in microstructure evolution enables one to provide the prediction on FIPs. The correlation between distributions of FIPs and their convex hulls are demonstrated. Distributions and convex hulls of FIPs provide important guidance in materials design, when certain grain size and texture information is known.

From the numerical examples we found that both PCA and KPCA provide reasonable predication to distributions of FIPs as well as their convex hulls. In the current work, however, PCA is more accurate than KPCA. As discussed earlier, two main reasons may apply: (1) the variation of initial samples is too small to show the non-linear nature of the microstructure input data; (2) the accuracy of the K nearest neighbor pre-imaging strategy adopted is not good enough to provide precise microstructure reconstruction; (3) the kernel selected here could not effectively reduce the non-linearity of the data. ASGC produces consistent predictions with MC but is computationally more efficient. Furthermore, the independence assumption of low-dimensional random variables may also be a source of inaccuracy for all stochastic simulations.

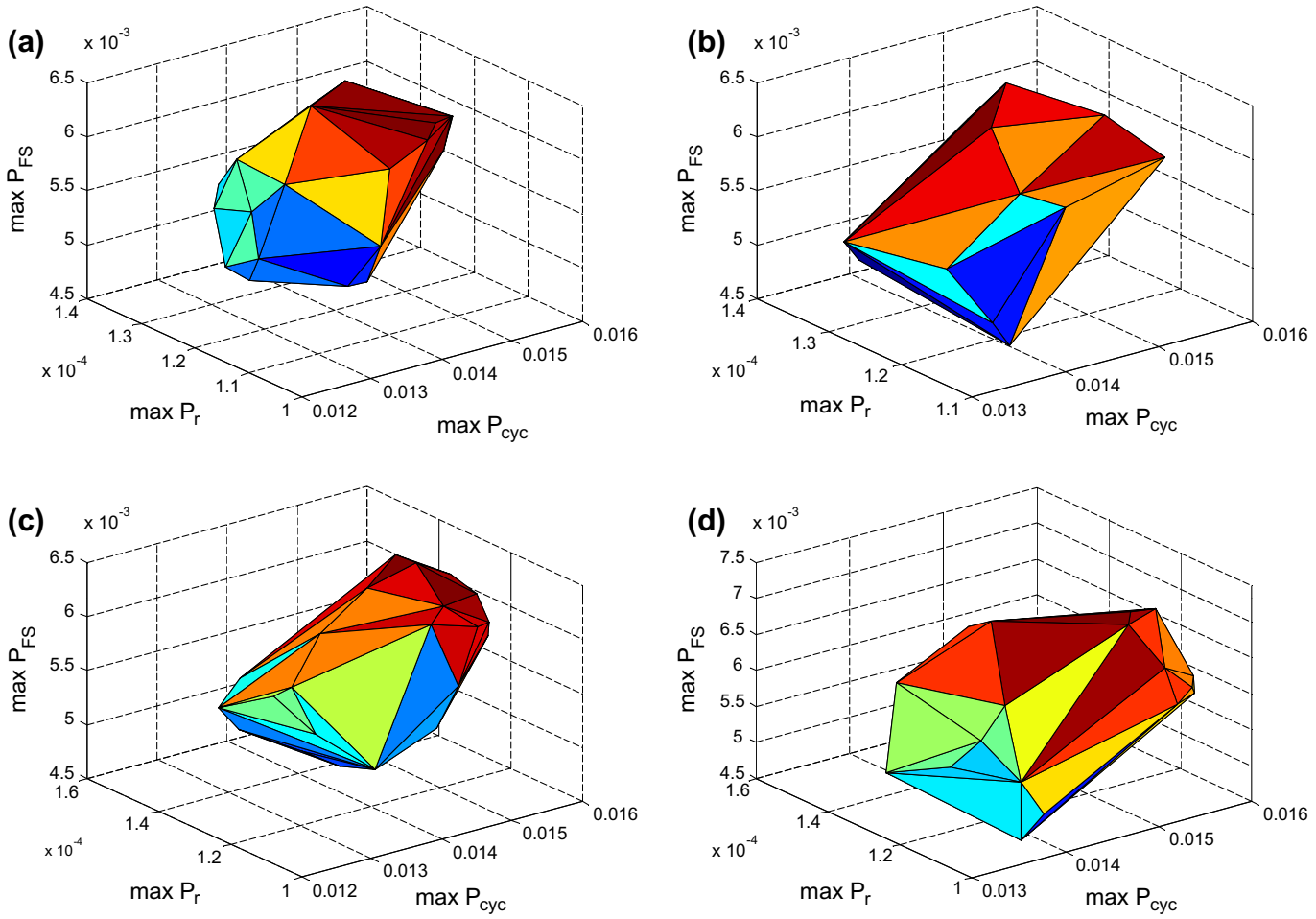

Fig. 25. Convex hulls of maximum FIPs constructed by 10,000 samples. The random source is texture and the reduced dimensionality is 4. (a) MC-PCA; (b) MC-KPCA; (c) ASGC-PCA; (d) ASGC-KPCA.

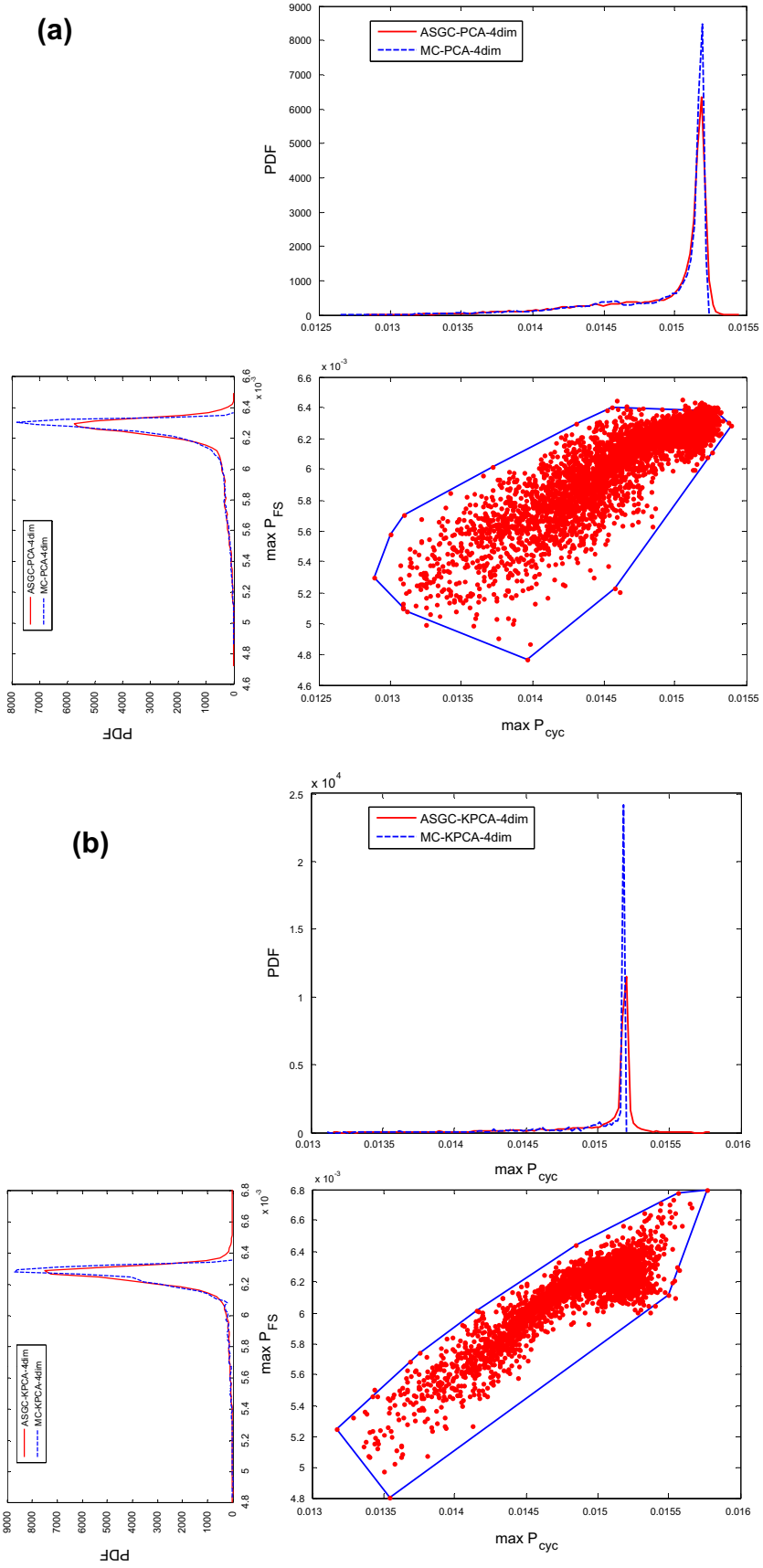

Fig. 26. 2D convex hull with enclosed sample points obtained by ASGC. Both ASGC and MC distributions corresponding to the chosen FIPs are also plotted to show the probability of occurrence of specific values. The random source is texture and the reduced dimensionality is 4. (a) *Max* P_{cyc} vs. *Max* P_{FS} when PCA is adopted; (b) *Max* P_{cyc} vs. *Max* P_{FS}, when KPCA is adopted.

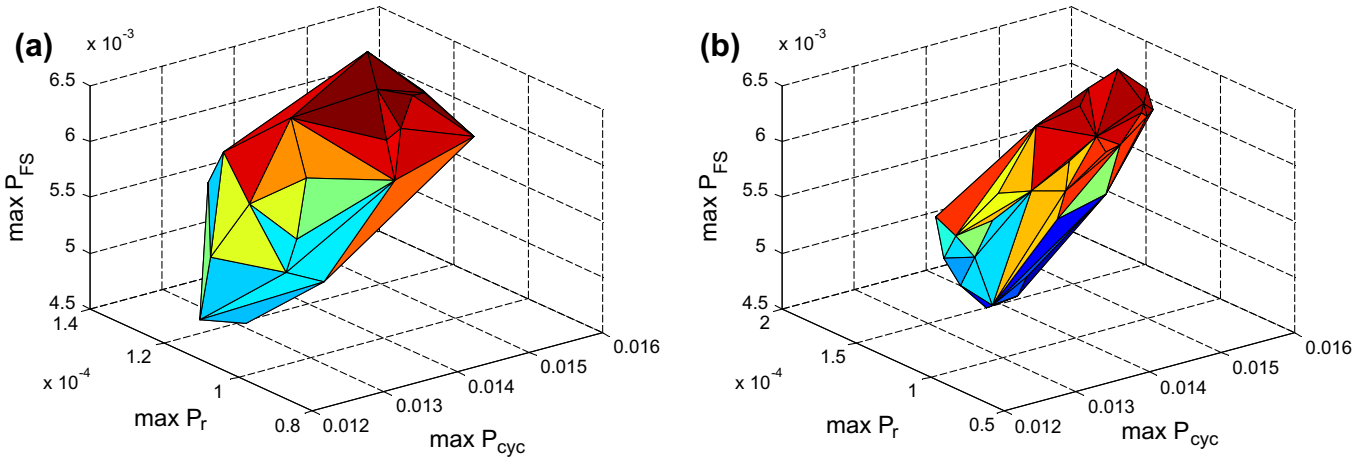

Fig. 27. Convex hulls of maximum FIPs constructed by 10,000 samples from ASGC. The random sources are texture and volume fractions of secondary and tertiary γ' precipitates. The reduced dimensionality of texture is 4, and the volume fractions are sampled from $\mathscr{U}(0.3, 0.5)$ and $\mathscr{U}(0.11, 0.14)$, respectively, for secondary and tertiary precipitates. (a) 3D convex hull of MC results; (b) 3D convex hull of ASGC results.

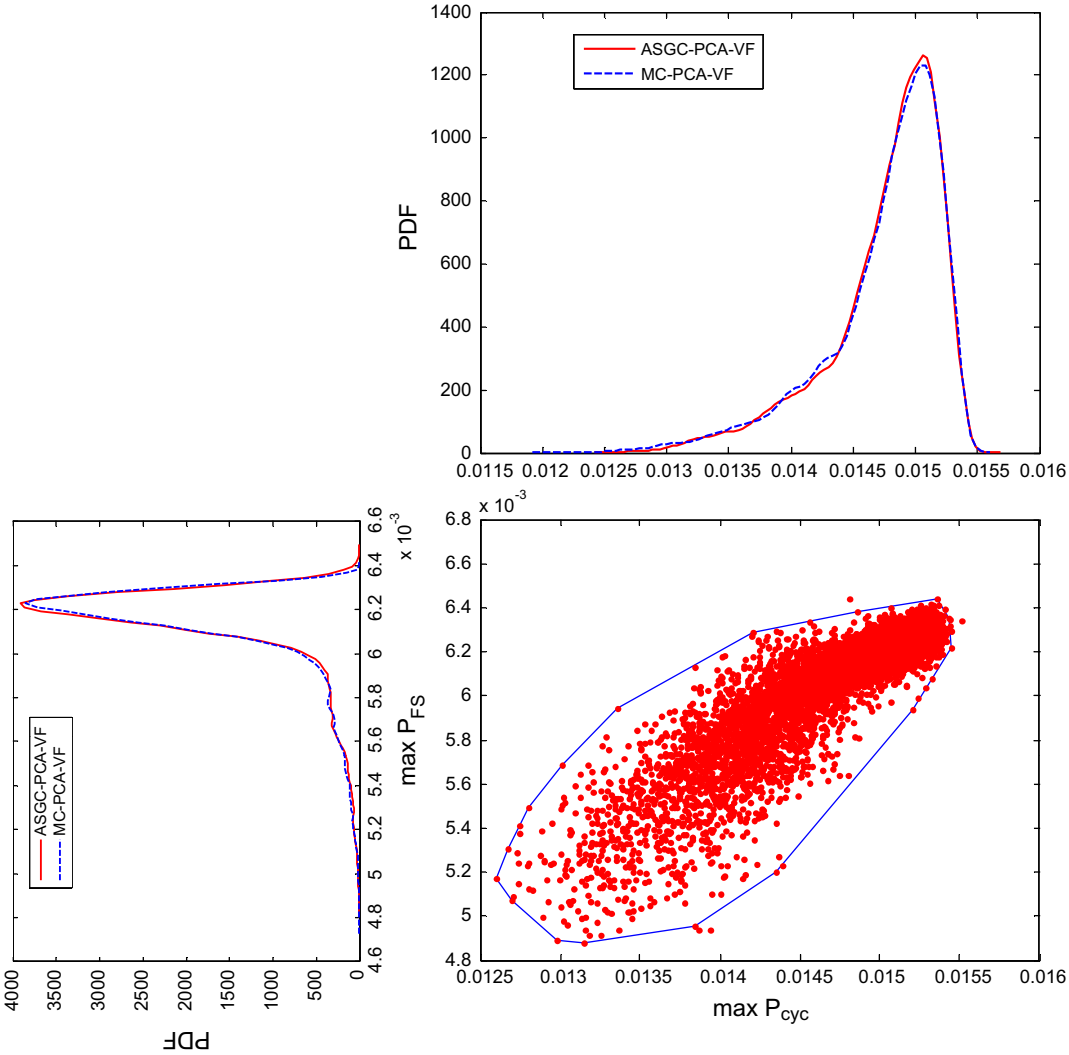

Fig. 28. 2D convex hull with enclosed sample points obtained by ASGC. The random sources are texture and volume fractions of secondary and tertiary γ' precipitates. The reduced dimensionality of texture is 4, and the volume fractions are sampled from $\mathscr{U}(0.3, 0.5)$ and $\mathscr{U}(0.11, 0.14)$, respectively, for secondary and tertiary precipitates.

In the current stochastic simulation, the modeling of the Ni-based superalloy microstructure does not take into account the interaction between grains as the crystal plasticity constitutive model is implemented using the Taylor approach for the purpose of efficiency. The predictions can be improved by adopting finite element (FE) model. However, this approach will be computationally very expensive. The self-consistent (VPSC) [47] approach taking into account stress compatibility is a potentially alternative method. Model reduction on realistic microstructures represented in the form of images is also of interest.

Acknowledgments

We acknowledge support from the Computational Mathematics program of AFOSR (Grant F49620-00-1-0373), the Materials Design and Surface Engineering program of the NSF (award CMMI-0757824), the Mechanical Behavior of Materials program Army Research Office (proposal to Cornell University No. W911NF0710519), the DOE Office of Science ASCR, and an OSD/AFOSR MURI09 award to Cornell University on uncertainty quantification.

References

[1] S. Sankaran, N. Zabaras, Acta Materialia 55 (7) (2007) 2279–2290.
[2] L. Anand, M. Kothari, Journal of the Mechanics and Physics of Solids 44 (4) (1996) 525–558.
[3] B. Kouchmeshky, N. Zabaras, Computational Materials Science 47 (2) (2009) 342–352.
[4] M. Loève, Probability Theory, fourth ed., Springer-Verlag, Berlin, 1977.
[5] R. Ghanem, P.D. Spanos, Stochastic Finite Elements: A Spectral Approach, Springer-Verlag, New York, 1991.
[6] B. Ganapathysubramanian, N. Zabaras, Journal of Computational Physics 225 (2007) 652–685.
[7] X. Ma, N. Zabaras, Journal of Computational Physics 228 (2009) 3084–3113.
[8] Z. Li, B. Wen, N. Zabaras, Computational Materials Science 49 (3) (2010) 568–581.
[9] B. Wen, Z. Li, N. Zabaras, Communications in Computational Physics 10 (3) (2011) 607–634.
[10] B. Ganapathysubramanian, N. Zabaras, Journal of Computational Physics 227 (2008) 6612–6637.
[11] R.C. Reed, The Superalloys: Fundamentals and Applications, Cambridge University Press, New York, 2006.
[12] E. Nembach, Particle Strengthening of Metals and Alloys, first ed., John Wiley & Sons, Inc., New York, 1997.
[13] V. Mohles, Philosophical Magazine, Part A 81 (2001) 971–990.
[14] V. Mohles, Materials Science and Engineering A 365 (1–2) (2004) 144–150.
[15] S.I. Rao, T.A. Parthasarathy, D.M. Dimiduk, P.M. Hazzledine, Philosophical Magazine 84 (30) (2004) 3195–3215.
[16] S.I. Rao, T.A. Parthasarathy, D.M. Dimiduk, P.M. Hazzledine, Philosophical Magazine Letters 86 (2006) 215–225.
[17] A. Vattré, B. Devincre, A. Roos, Intermetallics 17 (12) (2009) 988–994.
[18] E.P. Busso, F.T. Meissonnier, N.P. O'Dowd, Journal of the Mechanics and Physics of Solids 48 (11) (2000) 2333–2361.
[19] B. Fedelich, Computational Materials Science 16 (1–4) (1999) 248–258.
[20] B. Fedelich, International Journal of Plasticity 18 (1) (2002) 1–49.
[21] M.M. Shenoy, A.P. Gordon, D.L. McDowell, R.W. Neu, Journal of Engineering Materials and Technology 127 (3) (2005) 325–336.
[22] M.M. Shenoy, R.S. Kumar, D.L. McDowell, International Journal of Fatigue 27 (2) (2005) 113–127.
[23] R. Kumar, A. Wang, D. Mcdowell, International Journal of Fracture 137 (2006) 173–210.
[24] D. McDowell, F. Dunne, International Journal of Fatigue 32 (9) (2010) 1521–1542. emerging Frontiers in Fatigu.
[25] C.P. Przybyla, D.L. McDowell, International Journal of Plasticity 26 (3) (2010) 372–394.
[26] M. Shenoy, J. Zhang, D. McDowell, Fatigue & Fracture of Engineering Materials & Structures 30 (10) (2007) 889–904.
[27] G. Yagawa, H. Okuda, Archives of Computational Methods in Engineering 3 (1996) 435–512.
[28] M. Shenoy, Y. Tjiptowidjojo, D. McDowell, International Journal of Plasticity 24 (10) (2008) 1694–1730. special Issue in Honor of Jean-Louis Chaboch.
[29] I.T. Jolliffe, Principal Component Analysis, second ed., Springer-Verlag, New York, 2002.
[30] B. Schölkopf, A. Smola, K.-R. Müller, Neural Computation 10 (1998) 1299–1319.
[31] B. Schölkopf, A. Smola, Learning With Kernels, MIT Press, 2002.
[32] D. Xiu, G.E. Karniadakis, SIAM Journal on Scientific Computing 24 (2002) 619–644.
[33] D. Xiu, G.E. Karniadakis, Journal of Computational Physics 187 (2003) 137–167.
[34] X. Ma, N. Zabaras, Journal of Computational Physics 227 (2008) 8448–8471.
[35] V. Sundararaghavan, N. Zabaras, Statistical Analysis and Data Mining 1 (5) (2009) 306–321.
[36] F. Frank, Metallurgical and Materials Transactions A 19 (1988) 403–408.
[37] B. Ganapathysubramanian, N. Zabaras, Journal of Computational Physics 226 (1) (2007) 326–353.
[38] J.B. Tenenbaum, V.d. Silva, J.C. Langford, Science 290 (5500) (2000) 2319–2323.
[39] X. Ma, N. Zabaras, Journal of Computational Physics 230 (19) (2011) 7311–7331.
[40] J.-Y. Kwok, I.-H. Tsang, IEEE Transactions on Neural Networks 15 (2004) 1517–1525.
[41] G. Stefanou, A. Nouy, A. Clement, International Journal for Numerical Methods in Engineering 79 (2009) 127–155.
[42] Y. Rathi, S. Dambreville, A. Tannenbaum, Statistical shape analysis using kernel PCA, in: Image Processing: Algorithms and Systems, Neural Networks, and Machine Learning, SPIE, 2006, p. 60641B.
[43] M. Rosenblatt, Annals of Mathematical Statistics 23 (1952) 470–472.
[44] R.G. Ghanem, A. Doostan, Journal of Computational Physics 217 (2006) 63–81.
[45] W. Li, N. Zabaras, Computational Materials Science 44 (4) (2009) 1163–1177.
[46] C.B. Barber, D.P. Dobkin, H. Huhdanpaa, ACM Transactions on Mathematical Software 22 (4) (1996) 469–483.
[47] R.A. Lebensohn, G.R. Canova, Acta Materialia 45 (9) (1997) 3687–3694.